

Models for differential cross section in proton-proton scattering and their implications at ISR and LHC energies

Muhammad Saad Ashraf,¹ Nosheen Akbar,¹ and Sarwat Zahra²

¹*Department of Physics, COMSATS University Islamabad, Lahore Campus, Lahore, Pakistan.*

²*Department of Physics, DSNT, University of Education, Lahore, Pakistan.**

Few composite exponential models for the differential cross section ($\frac{d\sigma}{d|t|}$) are proposed to analyse the proton-proton (pp) elastic scattering at several energies. These proposed models are fitted to the data for pp elastic differential cross section reported at CERN-ISR, LHC, and extrapolated energies of other models. These models have produced important features including dip-bump structure and shrinkage of the forward peak. Position of the dip is also well produced by our models for all the data across a broad energy range of $\sqrt{s} = 23$ GeV, 23.5 GeV, 27.23 GeV, 30.7 GeV, 44.7 GeV, 52.8 GeV, 62.5 GeV, 200 GeV, 800 GeV, 2.76 TeV, 7 TeV, 8 TeV, 13 TeV, 14 TeV, 15 TeV, and 28 TeV. Employing these proposed models, elastic cross section (σ_{el}), inelastic cross section (σ_{tot}), and total cross section (σ_{tot}) are calculated at all the energies. Calculated results are compared with experimental data and theoretical results of other models. Implications of these results (obtained by models) related to the structure and dynamics of proton are discussed. The findings of this study emphasize the significance of combining theoretical and phenomenological approaches to accurately describe pp elastic scattering at high energies and provide significant information to future LHC experiments for the investigation of differential cross section.

Keywords: Elastic scattering, differential cross section, total elastic cross section, total cross section, inelastic cross section, QCD

I. INTRODUCTION

When high-energy hadron-hadron collisions take place, either new particles are produced, or they scatter elastically ($h_1 h_2 \rightarrow h_1 h_2$) with their quantum numbers conserved and without any production of new particles. In this study, we consider the latter case specified to proton-proton (pp) elastic scattering ($pp \rightarrow pp$). The pp scattering process has its foundational role in high-energy particle physics. It provides a unique and controlled laboratory to probe the non perturbative regime of Quantum Chromodynamics (QCD). This process is governed by strong interactions in principle and should be described by QCD. However, experimental data showed that the main features originate from non perturbative QCD. In the absence of rigorous solutions of QCD equations, our approach to high-energy hadronic processes at present is still at early stage of development. To gain understanding of these hadronic processes specifically the pp elastic scattering, various phenomenological approaches have been developed based on Regge Theory. Precise and consistent parametrization of elastic scattering data enhances our understanding of hadron structure and the emergence of collective phenomena like gluon saturation, making it an vital area of research in both theoretical and experimental high-energy physics. Study of pp elastic scattering allows researchers to have a direct access to the spatial and dynamical structure of the incoming protons through the measurement of the elastic differential cross section $\frac{d\sigma}{d|t|}$. The physical quantity $\frac{d\sigma}{d|t|}$ is among the most important quantities which have been calculated both experimentally and theoretically. It has been modeled in various contexts to describe the experimental data on pp elastic differential cross section so that significant insights can be obtained which can establish possible physical linkages with theoretical frameworks. The modeling of $\frac{d\sigma}{d|t|}$ is not only essential for interpreting collider data at CERN-Intersecting Storage Rings (ISR) and Large Hadron Collider (LHC) energies, but it also serves as a critical input for cosmic ray physics, hadronic Monte Carlo generators, and the development of theoretical frameworks such as eikonal models, Regge theory, and QCD-driven saturation approaches.

A. Experimental and Theoretical Contexts

Important pp elastic scattering measurements are carried out by CERN-ISR at different center of mass energies in GeV in the 1970s. Among the most significant characteristics of differential cross section that they observed are the

* msaadashraf99@gmail.com; nosheenakbar@cuilahore.edu.pk (corresponding author); sarwat.zahra@ue.edu.pk

diffractive peak, the dip-bump structure, and the gradual increase in the total cross section with increase in \sqrt{s} . Soft diffractive processes resulting from pomeron, reggeon, and meson exchanges are responsible for elastic scattering at low energies. According to ref. [1], soft diffractive interactions controlled by pomeron exchange within the Regge regime dominate elastic scattering at low momentum $|t| \leq 0.1 \text{ GeV}^2$. A change from soft pomeron-dominated scattering to the perturbative QCD (pQCD) regime at intermediate momentum $|t| \sim 1 - 2 \text{ GeV}^2$ [2] is indicated by deviations from simple exponential fits. At high momentum $|t| > 2 \text{ GeV}^2$, perturbative QCD effects and possible indications of parton saturation or color transparency become significant beyond the dip region, which can be understood from refs. [3–5]. For a broad momentum range of $|t| \approx 0.8\text{--}10 \text{ GeV}^2$, the differential cross sections for $\sqrt{s} = 23\text{--}63 \text{ GeV}$ at ISR energies have been measured in ref. [6].

Among the important advances, achieved by TOTEM Collaboration at LHC energies, the accurate measurements of pp elastic scattering are at $\sqrt{s} = 2.76, 7, 8, 13 \text{ TeV}$ under different experimental settings as described in refs. [7–11]. The sequence of TOTEM measurements revealed that the diffractive minimum and diffractive maximum, also known as dip and bump, are a continuous feature of the pp differential cross-section, in contrast to $\bar{p}p$ at high energies. By comparing pp and $\bar{p}p$ interactions, the D0 and TOTEM Collaborations recently discovered the C-odd exchange, sometimes referred to as the Odderon exchange [12]. High-precision measurements of the ρ parameter, elastic and total cross-sections have been made by the TOTEM Collaboration, revealing important aspects of elastic scattering at TeV energies. Other significant TeV-scale measurements done prior to TOTEM include the UA4 collaboration [13] [14], CDF collaboration [15], E710 collaboration [16–18], ATLAS experiment [19], and RHIC [20]. The vast amount of data gathered from these measurements has led to the development of several theoretical and phenomenological models [21–25]. However, the new TOTEM data from $\sqrt{s} = 2.76$ to 13 TeV [26] is not sufficiently explained by these models.

One of the most effective methods for examining the dynamical and spatial structure of the proton is the study of elastic pp scattering. Elastic processes give direct access to the spatial distribution of matter within the proton and contribute around one-fourth of the total cross section at high energy. According to ref.[27], the proton has a layered macrostructure: 1) a dense inner core made up of confined valence quarks and gluons; 2) a middle shell related to the distribution of baryonic charge; and 3) an outer peripheral region dominated by meson cloud contributions ($q\bar{q}$ condensates). In elastic collisions, the momentum transfer is related to the transverse distance (b) by ($b \sim 1/\sqrt{|t|}$). Thus, higher- $|t|$ values probe deeper into the baryonic core and the valence quark region, whereas low- $|t|$ elastic scattering probes the large-distance, low-density mesonic cloud. When momentum transfers are low, the differential cross section $\frac{d\sigma}{dt} \simeq e^{Bt}$ with B as the slope parameter describing the transverse extension of the interaction region, exhibits approximately exponential behavior. The deviations from pure exponential behavior become evident as t grows, suggesting the inclusion of interference effects between various spatial components and internal proton layers. Quark-quark scattering dominates the deep elastic scattering domain above $|t| \gtrsim 4 \text{ GeV}^2$.

As the center of mass energy is raised from ISR to LHC energies, the proton becomes more absorbent and black, its interaction profile becomes more peripheral, and its effective interaction radius grows [28]. At ISR energies, a relatively compact proton interaction region is dominated by valence quarks and sea quarks with a moderate density of gluons. As energy increases approaching LHC scales, the interaction radius (R_{int}) increases due to the growth of gluon densities at small Bjorken- x . As the slope parameter $B(s)$ rises from around 14 GeV^{-2} (ISR) to over 21.19 GeV^{-2} (LHC), this growth is evident in the exponential fit to the elastic cross-section [29]. The "shrinkage of the forward peak" and the deepening and shifting of the diffractive dip in $d\sigma/dt$ towards lower $|t|$ values are the empirically observed manifestations of it. The gluon density within the proton increases considerably at LHC energy, resulting in nonlinear QCD processes such as gluon recombination and saturation [30]. At ISR energies, there is uniformity in the impact-parameter profile of proton. On the other hand, different core-corona structures are formed at LHC energies due to double-parton interactions. The proton is frequently described as a spherically symmetric particle at ISR, but at LHC, it takes on an asymmetric form due to event-by-event fluctuations in the gluon distributions that depend on the impact parameter.

In recent decades, researchers have proposed a wide range of theoretical and phenomenological models to represent pp elastic scattering data ranging ISR and LHC energies. However, more sophisticated models have been required to achieve full agreement with experimental results. The energy dependence of total cross-sections and elastic scattering employing pomeron exchange are described in ref.[1]. The non-exponential behavior in the differential cross-section at low $|t|$, however, is not amenable to fitting by traditional Regge models. In ref.[31], the dip-bump structure in the differential cross section is described only at low energies using a dipole pomeron based formalism. In pp and $\bar{p}\bar{p}$ elastic scattering at low momentum transfers, the interplay between electromagnetic and hadronic interactions has been extensively studied using the Coulomb-Nuclear Interference (CNI) model, which is developed by Cahn in 1980 [32]. The CNI model, which included nuclear and Coulomb amplitudes in an eikonal formalism, offered a foundation for calculating the hadronic phase shift. The CNI model is further utilized and improved in ref. [34]. At ISR and LHC

energies, limitations of the CNI model related to the Coulomb phase, spin effects, and nonlinear QCD corrections also exist. In order to better fit the experimental results, the TOTEM Collaboration in [35] employed quadratic and cubic polynomial parameterizations in the exponent at $\sqrt{s} = 8$ TeV in the range of $0.027 < |t| < 0.2$ GeV². A number of studies that employed these parametrizations are included in the refs. [36–38]. In ref. [39], several parametrizations are developed to explain the differences in between pp and $\bar{p}p$ scattering and provided qualitative agreement for exchange of Odderon. At high energies, the gluon density inside the proton grows significantly, and saturation models quite explicitly describe this regime. A QCD-based framework that generalizes parton distributions (GPDs) extends to both soft and hard interactions which is provided by the HEGS (High Energy Generalized Structure) for pp elastic scattering refs.[40, 41]. According to refs.[42, 43], the model described two-gluon and three-gluon exchange contributions and matched the ISR and LHC data, as well as the $\sigma_{tot}(s)$ and $B(s)$. The HEGS model still has to be refined in terms of unitarization and Odderon contributions in order to accurately describe the scattering amplitude. In ref. [44], elastic pp scattering in the Regge regime is investigated in a holographic QCD model, and consistent outcomes have been obtained using 13 TeV TOTEM data. An empirical model that is developed and proved to be in good agreement with LHC and ISR data is based on the early work of Phillips and Barger [45]. An exponential shape of the differential cross-section is assumed by the Phillips-Barger Model (PB), which may be used to determine the parton distribution inside the proton. The recent pp and $\bar{p}p$ elastic scattering data at $\sqrt{s} = 8$ and 13 TeV are represented by an improved Phillips-Barger model in ref.[46], which also highlighted the significance of the Odderon exchange. Elastic scattering is described at ISR energies [47] and at an LHC energy of $\sqrt{s} = 7$ TeV [48] by modifying the Bialas-Bzdak model, which considered the proton as a bound state of a quark and a diquark. A constant bump-to-dip ratio of the differential cross-section $\frac{d\sigma_{el}}{dt}$ at the ISR and LHC energies is found in the context of geometrical scaling in ref. [49]. The constant bump-to-dip ratio and a family of scaling rules are also found at the LHC in ref. [50].

A precise parametrization and fitting of the differential cross-section in pp elastic scattering at ISR and LHC energies has important implications for hadronic interactions, QCD dynamics, and proton structure. The Coulomb-Nuclear Interference (CNI) phase, which is essential for understanding low- $|t|$ behavior, the elastic slope parameter $B(s)$, which probes the interaction range, and the total cross-section through the Optical Theorem can all be extracted using these expressions [1][26][33][51]. Fits can reveal information on the spatial distribution of interaction region of proton, demonstrating an energy-dependent increase in the radius of proton, through the slope parameter $B(s)$. By using Fourier transforms, these parametrizations allow in developing a model of the impact parameter distribution, which can provide information about the spatial structure of proton [52]. Additionally, refined Parton Distribution Functions (PDFs) [53], improve collider luminosity calibration [26, 54], and are vital for high-energy cosmic-ray interactions [55, 56]. They make it easier to examine non-perturbative QCD models, such as saturation and eikonal frameworks [57][58], and to extrapolate cross-sections to future collider energies, such as the FCC [59]. Applications such as astroparticle research, neutrino physics, and machine learning-based cross-section predictions can all benefit from these parameterizations [60]. For the advancement of theoretical and experimental high-energy physics and the investigation of strong interaction dynamics, continuous advancement is very crucial. It is emphasized that the only way to provide substantial support for theoretical advancements is to conduct a global comparative analysis of various methodologies, parametrizations, and solutions in order to obtain empirical data on what is universal across every context. The offered method and results aim to advance research into inverse problems in high-energy elastic hadron-hadron scattering.

In order to explain the recent pp elastic scattering measurements by the TOTEM Collaboration at LHC and previously by the CERN Intersecting Storage Rings (ISR) and their extrapolations, we present a number of models of elastic differential cross section $\frac{d\sigma}{d|t|}$ as a function of s and $|t|$, the magnitude of the four-momentum transfer squared based on empirical observations.

We describe our methodical approach towards modeling the elastic differential cross section $\frac{d\sigma}{d|t|}$ in section II. The results of fitting of our models with all the data are shown in section III. The calculations of the elastic, total, and inelastic cross sections by our models are written in this section. The χ^2 and other error measures for differential cross section model fitting and total elastic cross section are also written in section III. In section III, the potential physical significance of our models and how they could relate to other models are also explored. Section IV provides the conclusion of this study. Additionally, section V offers recommendations for future investigations in the directions highlighted by this study.

II. METHODOLOGY

In this study, seven different models based on their ability to reproduce key features of the differential cross-section, including the forward peak, diffractive dip, and large- $|t|$ behavior are developed to fit the ISR and TOTEM elastic pp differential cross-section data. The ISR data at low energies: $\sqrt{s} = 23, 23.5, 30.7, 44.7, 52.8, 62.5$ GeV covered a

broad range of momentum transfer squared $0 < |t| < 9.75 \text{ GeV}^2$ refs. [6][61]. The data from TOTEM experiment at higher energies: $\sqrt{s} = 2.76, 7, 8, 13 \text{ TeV}$ from refs. [7–11], contained precise results of the differential cross-section at a low range of $0.037 < |t| < 4.03 \text{ GeV}^2$ values. Non-linear fitting for the models is performed for both the two datasets and the parameters of the models of the elastic differential cross section are determined. The models are also fitted to extrapolated results at future LHC energies of 14, 15 and 28 TeV of ref. [47]. Predicted results at 200 GeV and 800 GeV of ref. [62], and at 27.43 GeV of [63] are also fitted by these models.

For the non-linear fitting, the data (in GeV) is taken for $|t|$ in following ranges: at 23 GeV, the range is $0.04 \leq |t| \leq 3.6 \text{ GeV}^2$; at 23.5 GeV, the range is $0.042 \leq |t| \leq 5.75 \text{ GeV}^2$; at 27.43 GeV, the range is $0.45400 \leq |t| \leq 9.87720 \text{ GeV}^2$; at 30.7 GeV, the range is $0.00106 \leq |t| \leq 5.75 \text{ GeV}^2$; at 44.7 GeV, the range is $0.00099 \leq |t| \leq 7.25 \text{ GeV}^2$; at 52.8 GeV, the range is $0.00126 \leq |t| \leq 9.75 \text{ GeV}^2$; at 62.5 GeV, the range is $0.00167 \leq |t| \leq 6.25 \text{ GeV}^2$; at 200 GeV, the range is $0.02625 \leq |t| \leq 9.81090 \text{ GeV}^2$; at 800 GeV, the range is $0.00600 \leq |t| \leq 9.97059 \text{ GeV}^2$.

The data (in TeV) is taken for $|t|$ in following ranges: at 2.76 TeV, the range is $0.3825 \leq |t| \leq 0.7625 \text{ GeV}^2$; at 7 TeV, the range is $0.381 \leq |t| \leq 2.543 \text{ GeV}^2$; at 8 TeV, the range is $0.20778 \leq |t| \leq 1.86469 \text{ GeV}^2$; at 13 TeV, the range is $0.03926 \leq |t| \leq 4.03464 \text{ GeV}^2$; at 14 TeV, the range is $0.00711 \leq |t| \leq 2.14128 \text{ GeV}^2$; at 15 TeV, the range is $0.00718 \leq |t| \leq 2.47130 \text{ GeV}^2$; at 28 TeV, the range is $0.01432 \leq |t| \leq 2.47856 \text{ GeV}^2$.

A. Models for the Differential Cross Section

Different parametrizations which are constructed as multi-component exponential structures for modeling of the differential cross section for pp elastic scattering are presented here. These models represent the composite behavior of the scattering amplitude in different kinematic regimes to fit the data. In these models scaling-like factors (s/s_0) have been introduced with dimensionless exponents, η and μ to fit the data. In this factor, the quantity s_0 is taken to be of the order of a GeV^2 , because this is the typical scale associated with high-energy hadronic reactions. Such s dependent factors have been used to approximate the differential cross sections of various scattering phenomena in ref. [64]. These factors are also reminiscent of the low- $|t|$ ($|t| < 1 \text{ GeV}^2$) form of the pp and $p\bar{p}$ elastic differential cross section model of ref. [4] in which single pomeron (\mathbb{P}) and double pomeron exchanges ($\mathbb{P}\mathbb{P}$) have been expressed in terms of their trajectories. This model describes pp elastic scattering in terms of pomeron coupling with the separate valence quarks of proton. For better understanding and correlation purposes with this low- $|t|$ model, we mention its expression as follows

$$\frac{d\sigma}{dt} = \left(\frac{3\beta_P F_1(t)}{4\pi} \right)^4 (s/s_0)^{2\alpha_P(t)-2}. \quad (1)$$

The proton form factor $F_1(t)$ is parameterized as $(F_1(t))^2 = Ae^{at} + Be^{bt} + Ce^{ct}$ for calculational convenience and the trajectory for the pomeron exchange is given as $\alpha_P(t) = 1 + \epsilon_P + \alpha'_P t$. The constant β_P originated from pomeron-exchange contribution to quark-quark scattering. Keeping these facts in view, we have introduced simple energy dependent generalized parameters ($A(s)$ and $B(s)$) that will appear in our models as $A(s) = A_0(s/s_0)^\eta$ and $B(s) = B_0(s/s_0)^\mu$ respectively. This form not only offers lesser number of parameters but also reduces statistical errors in fitting. Each model is distinct and involves several free parameters that are determined by fitting with all the data. In this study, the analysis of the data is performed by non-linear fitting, the final outcome profoundly depends on the choice of initial values of the free parameters which are not known. Therefore reaching a unique solution is not certain but only one or more possible solutions. The most optimal set of parameters values for each model across a center-of-mass energy is the set of values for which the curve fitting and the calculations can show most agreement with reference values. Our models differ from traditional Regge models which usually involve a large numbers of parameters. We now describe our models as follows.

1. Model 1

This simple exponential model is introduced in the following form:

$$\frac{d\sigma(s,t)}{dt} = \sum_{i=1}^m A_i(s,t) e^{-B_i(s,t)}. \quad (2)$$

with $i = 1, 2, 3, \dots, m$. If $m = 4$ then it can be expanded in the following form with four exponential terms.

$$\frac{d\sigma(s, t)}{dt} = A_1(s, t)e^{-B_1(s, t)} + A_2(s, t)e^{-B_2(s, t)} + A_3(s, t)e^{-B_3(s, t)} + A_4(s, t)e^{-B_4(s, t)}. \quad (3)$$

Where $A_1(s, t), A_2(s, t), A_3(s, t), A_4(s, t), B_1(s, t), B_2(s, t), B_3(s, t)$, and $B_4(s, t)$ are functions of s and t . These functions are $A_1(s, t) = A_1(s)t^0$, $A_2(s, t) = A_2(s)t^0$, $A_3(s, t) = A_3(s)t^0$, and $A_4(s, t) = A_4(s)t^0$. And $B_1(s, t) = B_1(s)t$, $B_2(s, t) = B_2(s)t$, $B_3(s, t) = B_3(s)t$, and $B_4(s, t) = B_4(s)t$. We define $A(s)$ parameters as $A_1(s) = A_1(s/s_0)^\eta$, $A_2(s) = A_2(s/s_0)^\eta$, $A_3(s) = A_3(s/s_0)^\eta$, and $A_4(s) = A_4(s/s_0)^\eta$. The $B(s)$ parameters are given as $B_1(s) = B_1(s/s_0)^\mu$, $B_2(s) = B_2(s/s_0)^\mu$, $B_3(s) = B_3(s/s_0)^\mu$ and $B_4(s) = B_4(s/s_0)^\mu$. After substituting all the values of $A(s)$ and $B(s)$ parameters, we obtain the following form of this model for the fitting.

$$\frac{d\sigma(s, t)}{dt} = (s/s_0)^\eta (A_1 e^{-B_1(s/s_0)^\mu t} + A_2 e^{-B_2(s/s_0)^\mu t} + A_3 e^{-B_3(s/s_0)^\mu t} + A_4 e^{-B_4(s/s_0)^\mu t}). \quad (4)$$

The the parameters $A_1, A_2, A_3, A_4, B_1, B_2, B_3, B_4, \eta$ and μ are treated as free parameters which are determined through fitting. The values of all the parameters of this model are given in Table 1.

2. Model 2

This exponential model is given in the following form.

$$\frac{d\sigma(s, t)}{dt} = \sum_{i=1}^m A_i(s, t)e^{-B_i(s, t)} (1 + \alpha e^{-C_j(s, t)})^n. \quad (5)$$

with $i = 1, 2, 3, \dots, m$. Here we take $m = 4$, and when $i = 1$ then $j = n = 1$. And when $i = 2, 3$, and 4 then $n = 0$. Then the model takes the following form.

$$\frac{d\sigma(s, t)}{dt} = A_1(s, t)e^{-B_1(s, t)} (1 + \alpha e^{-C_1(s, t)}) + A_2(s, t)e^{-B_2(s, t)} + A_3(s, t)e^{-B_3(s, t)} + A_4(s, t)e^{-B_4(s, t)t}. \quad (6)$$

Here $A_1(s, t), A_2(s, t), A_3(s, t), A_4(s, t), B_1(s, t), C_1(s, t), B_2(s, t), B_3(s, t)$, and $B_4(s, t)$ are functions of s and t . These functions are $A_1(s, t) = A_1(s)t^0$, $A_2(s, t) = A_2(s)t^0$, $A_3(s, t) = A_3(s)t^0$, and $A_4(s, t) = A_4(s)t^{-m}$. And $B_1(s, t) = B_1(s)t$, $C_1(s, t) = C_1(s)t$, $B_2(s, t) = B_2(s)t$, $B_3(s, t) = B_3(s)t$, and $B_4(s, t) = B_4(s)t$. We define $A(s)$ parameters as $A_1(s) = A_1(s/s_0)^\eta$, $A_2(s) = A_2(s/s_0)^\eta$, $A_3(s) = A_3(s/s_0)^\eta$ and $A_4(s) = A_4(s/s_0)^\eta$. The $B(s)$ parameters are defined as $B_1(s) = B_1(s/s_0)^\mu$, $C_1(s) = C_1(s/s_0)^\mu$, $B_2(s) = B_2(s/s_0)^\mu$, $B_3(s) = B_3(s/s_0)^\mu$ and $B_4(s) = B_4(s/s_0)^\mu$. After substituting $A(s)$ and $B(s)$ parameters, we obtain the following form of this model for fitting.

$$\frac{d\sigma(s, t)}{dt} = (s/s_0)^\eta (A_1 e^{-B_1(s/s_0)^\mu t} (1 + \alpha e^{-C_1(s/s_0)^\mu t}) + A_2 e^{-B_2(s/s_0)^\mu t} + A_3 e^{-B_3(s/s_0)^\mu t} + A_4 e^{-B_4(s/s_0)^\mu t} t^{-m}). \quad (7)$$

Here the parameters $A_1, A_2, A_3, A_4, B_1, B_2, B_3, B_4, C_1, \alpha, \eta, m$, and μ are treated as free parameters which have been determined through fitting. The first two terms have the same amplitude coefficient A_1 and the $e^{-B_1(s/s_0)^\mu t}$ factors. A power law factor t^{-m} is combined with exponential damping in the last term for better fitting. This factor allows the model to smoothly transition from soft diffraction (low- $|t|$) to hard scattering behavior (high- $|t|$). The values of all the parameters of this model are given in Table 2.

3. Model 3

This exponential model with a quadratic modulation factor is given in the following form.

$$\frac{d\sigma(s, t)}{dt} = \sum_{i=1}^m A_i(s, t)e^{-B_i(s, t)} ((1 - \alpha t/t_0)^2)^j. \quad (8)$$

with $i = 1, 2, \dots, m$ and $m = 4$. With the condition, when $i = 2$ then $j = 1$, and when $i = 1, 3$, and 4 then $j = 0$, we arrive at the following form.

$$\frac{d\sigma(s, t)}{dt} = A_1(s, t)e^{-B_1(s, t)} + A_2(s, t)e^{-B_2(s, t)}(1 - \alpha t/t_0)^2 + A_3(s, t)e^{-B_3(s, t)} + A_4(s, t)e^{-B_4(s, t)}. \quad (9)$$

Where $A_1(s, t)$, $A_2(s, t)$, $A_3(s, t)$, $A_4(s, t)$, $B_1(s, t)$, $B_2(s, t)$, $B_3(s, t)$, and $B_4(s, t)$ are functions of s and t . The functions are $A_1(s, t) = A_1(s)t^0$, $A_2(s, t) = A_2(s)t^0$, $A_3(s, t) = A_3(s)t^0$, and $A_4(s, t) = A_4(s)t^{-m}$. And $B_1(s, t) = B_1(s)t$, $B_2(s, t) = B_2(s)t$, $B_3(s, t) = B_3(s)t$, and $B_4(s, t) = B_4(s)t$. We define $A(s)$ parameters as $A_1(s) = A_1(s/s_0)^\eta$, $A_2(s) = A_2(s/s_0)^\eta$, $A_3(s) = A_3(s/s_0)^\eta$ and $A_4(s) = A_4(s/s_0)^\eta$. The $B(s)$ parameters are defined as $B_1(s) = B_1(s/s_0)^\mu$, $B_2(s) = B_2(s/s_0)^\mu$, $B_3(s) = B_3(s/s_0)^\mu$ and $B_4(s) = B_4(s/s_0)^\mu$. After substituting the $A(s)$ and $B(s)$ parameters, we obtain the following form of this model which is used for fitting.

$$\frac{d\sigma(s, t)}{dt} = (s/s_0)^\eta (A_1 e^{-B_1(s/s_0)^\mu t} + A_2 e^{-B_2(s/s_0)^\mu t} (1 - \alpha t/t_0)^2 + A_3 e^{-B_3(s/s_0)^\mu t} + A_4 e^{-B_4(s/s_0)^\mu t} t^{-m}). \quad (10)$$

Here the parameters $A_1, A_2, A_3, A_4, B_1, B_2, B_3, B_4, \alpha, m, \eta$, and μ are free parameters which have been determined through fitting the data at all the energies. This exponential model contains a quadratic modulation factor $(1 - \alpha t/t_0)^2$ in the second exponential term. This factor is zero when $t = t_0/\alpha$. When $t = 0$, the factor is close to 1, and the exponential dominates. As t increases, the polynomial suppresses the exponential behavior depending on the sign of α thus affecting the dip-bump region. At high t values this factor is useful to significantly suppress or enhance the tail behavior with changing the low- $|t|$ fit. The last exponential term contains a power law factor t^{-m} . For small t , t^{-m} can be large if $m > 0$, but the exponential term may dominate when $B_4(s/s_0)^\mu t \rightarrow 0$. For large t , t^{-m} becomes small but this may slow the overall decay if the exponential is decreasing too fast. The values of all the parameters of this model are given in Table 3.

4. Model 4

This exponential model with two quadratic modulation factors is written in the following form

$$\frac{d\sigma(s, t)}{dt} = \sum_{i=1}^m A_i(s, t)e^{-B_i(s, t)}(1 - \alpha t/t_0)^{2j}(1 - \beta t/t_0)^{2k}. \quad (11)$$

with $i = 1, 2, 3, \dots, m$, and $j = 0, 1$ and $k = 0, 1$. We take $m = 4$ and with the conditions: 1) For $i = 1, j = 1$, and for $i = 2, 3$, and $4, j = 0$, and 2) For $i = 2, k = 1$, and for $i = 1, 3$, and $4, k = 0$, we arrive at the following form of this model.

$$\frac{d\sigma(s, t)}{dt} = A_1(s, t)e^{-B_1(s, t)}(1 - \alpha t/t_0)^2 + A_2(s, t)e^{-B_2(s, t)}(1 - \beta t/t_0)^2 + A_3(s, t)e^{-B_3(s, t)} + A_4(s, t)e^{-B_4(s, t)}. \quad (12)$$

Here $A_1(s, t)$, $A_2(s, t)$, $A_3(s, t)$, $A_4(s, t)$, $B_1(s, t)$, $B_2(s, t)$, $B_3(s, t)$, and $B_4(s, t)$ are functions of s and t . These functions are $A_1(s, t) = A_1(s)t^0$, $A_2(s, t) = A_2(s)t^0$, $A_3(s, t) = A_3(s)t^0$, and $A_4(s, t) = A_4(s)t^0$. And $B_1(s, t) = B_1(s)t$, $B_2(s, t) = B_2(s)t$, $B_3(s, t) = B_3(s)t$, and $B_4(s, t) = B_4(s)t$. The $A(s)$ parameters are $A_1(s) = A_1(s/s_0)^\eta$, $A_2(s) = A_2(s/s_0)^\eta$, $A_3(s) = A_3(s/s_0)^\eta$ and $A_4(s) = A_4(s/s_0)^\eta$. The $B(s)$ parameters are given as $B_1(s) = B_1(s/s_0)^\mu$, $B_2(s) = B_2(s/s_0)^\mu$, $B_3(s) = B_3(s/s_0)^\mu$ and $B_4(s) = B_4(s/s_0)^\mu$. After substituting the $A(s)$ and $B(s)$ parameters, we obtain the following form of this model.

$$\frac{d\sigma(s, t)}{dt} = (s/s_0)^\eta (A_1 e^{-B_1(s/s_0)^\mu t} (1 - \alpha t/t_0)^2 + A_2 e^{-B_2(s/s_0)^\mu t} (1 - \beta t/t_0)^2 + A_3 e^{-B_3(s/s_0)^\mu t} + A_4 e^{-B_4(s/s_0)^\mu t}). \quad (13)$$

Here the parameters $A_1, A_2, A_3, A_4, B_1, B_2, B_3, B_4, \alpha, \beta, t_0, \eta$, and μ are treated as free parameters which have been determined through fitting the data at all the energies. This model contains mainly four exponential terms with two quadratic modulation factors, $(1 - \alpha t/t_0)^2$ and $(1 - \beta t/t_0)^2$ multiplied with the first and second terms respectively. These factors become zero when $t = t_0/\alpha$ and $t = t_0/\beta$. When $t = 0$, these factors are one and preserve the exponential factors. The values of all the parameters of this model are given in Table 4.

5. Model 5

This exponential model with saturation like correction factor is given in the following form

$$\frac{d\sigma(s,t)}{dt} = \sum_{i=1}^m A_i(s,t) e^{-B_i(s,t)} (1-t/t_0)^{pj}. \quad (14)$$

with $i = 1, 2, \dots, m$. We take $m = 4$ and with condition: when $i = 3$ then $j = 1$ and when $i = 1, 2$ and 4 , then $j = 0$, we arrive at the following form of this model.

$$\frac{d\sigma(s,t)}{dt} = A_1(s,t) e^{-B_1(s,t)} + A_2(s,t) e^{-B_2(s,t)} + A_3(s,t) e^{-B_3(s,t)} (1-t/t_0)^p + A_4(s,t) e^{-B_4(s,t)}. \quad (15)$$

Here $A_1(s,t)$, $A_2(s,t)$, $A_3(s,t)$, $A_4(s,t)$, $B_1(s,t)$, $B_2(s,t)$, $B_3(s,t)$, and $B_4(s,t)$ are functions of s and t . These functions are $A_1(s,t) = A_1(s)t^{-m}$, $A_2(s,t) = A_2(s)t^{-n}$, $A_3(s,t) = A_3(s)t^0$, and $A_4(s,t) = A_4(s)t^0$. And $B_1(s,t) = B_1(s)t$, $B_2(s,t) = B_2(s)t$, $B_3(s,t) = B_3(s)t$, and $B_4(s,t) = B_4(s)t$. The $A(s)$ parameters are $A_1(s) = A_1(s/s_0)^\eta$, $A_2(s) = A_2(s/s_0)^\eta$, $A_3(s) = A_3(s/s_0)^\eta$ and $A_4(s) = A_4(s/s_0)^\eta$. The $B(s)$ parameters are given as $B_1(s) = B_1(s/s_0)^\mu$, $B_2(s) = B_2(s/s_0)^\mu$, $B_3(s) = B_3(s/s_0)^\mu$ and $B_4(s) = B_4(s/s_0)^\mu$. After substituting the values of the $A(s)$ and $B(s)$ parameters we obtain the following form of this model for fitting.

$$\frac{d\sigma(s,t)}{dt} = (s/s_0)^\eta (A_1 e^{-B_1(s/s_0)^\mu t} t^{-m} + A_2 e^{-B_2(s/s_0)^\mu t} t^{-n} + A_3 e^{-B_3(s/s_0)^\mu t} (1-t/t_0)^p + A_4 e^{-B_4(s/s_0)^\mu t}). \quad (16)$$

Here the parameters $A_1, A_2, A_3, A_4, B_1, B_2, B_3, B_4, m, n, \eta, \mu$, and p are free parameters which have been determined through fitting the data at all the energies. The parameter t_0 is a reference momentum scale (in GeV^2) controlling the onset of the saturation term. The first two terms combine exponential damping with power-law behavior, fitting the forward peak and early falloff at low and intermediate t value, respectively. The third term contains a saturation like correction factor $(1-t/t_0)^p$ which becomes significant at the mid- t region and helps to describe the dip-bump structure at higher energies. The last exponential term accounts for the large- t tail of the cross section as it provides a smooth decay at high t . The values of all the parameters of this model are given in Table 5.

6. Model 6

This exponential model with logarithmic correction factor is given in the the following form

$$\frac{d\sigma(s,t)}{dt} = \sum_{i=1}^m A_i(s,t) e^{-B_i(s,t)} (\text{Log}(1 + \alpha t/t_0))^j. \quad (17)$$

with $i = 1, 2, \dots, m$ and $m = 4$. By using the condition, when $i = 2$ then $j = 1$ and when $i = 1, 3$ and 4 , $j = 0$, we arrive at the following form of this model.

$$\frac{d\sigma(s,t)}{dt} = A_1(s,t) e^{-B_1(s,t)} + A_2(s,t) e^{-B_2(s,t)} \text{Log}(1 + \alpha t/t_0) + A_3(s,t) e^{-B_3(s,t)} + A_4(s,t) e^{-B_4(s,t)}. \quad (18)$$

Here $A_1(s,t)$, $A_2(s,t)$, $A_3(s,t)$, $A_4(s,t)$, $B_1(s,t)$, $B_2(s,t)$, $B_3(s,t)$, and $B_4(s,t)$ are functions of s and t . These functions are $A_1(s,t) = A_1(s)t^{-m}$, $A_2(s,t) = A_2(s)t^{-n}$, $A_3(s,t) = A_3(s)t^0$, and $A_4(s,t) = A_4(s)t^0$. And $B_1(s,t) = B_1(s)t$, $B_2(s,t) = B_2(s)t$, $B_3(s,t) = B_3(s)t$, and $B_4(s,t) = B_4(s)t$. The $A(s)$ parameters are $A_1(s) = A_1(s/s_0)^\eta$, $A_2(s) = A_2(s/s_0)^\eta$, $A_3(s) = A_3(s/s_0)^\eta$ and $A_4(s) = A_4(s/s_0)^\eta$. The $B(s)$ parameters are given as $B_1(s) = B_1(s/s_0)^\mu$, $B_2(s) = B_2(s/s_0)^\mu$, $B_3(s) = B_3(s/s_0)^\mu$ and $B_4(s) = B_4(s/s_0)^\mu$. After substituting the values of the $A(s)$ and the $A(s)$ parameters, we obtain the following form of this model for fitting.

$$\frac{d\sigma(s,t)}{dt} = (s/s_0)^\eta (A_1 e^{-B_1(s/s_0)^\mu t} t^{-m} + A_2 e^{-B_2(s/s_0)^\mu t} t^{-n} \text{Log}(1 + \alpha t/t_0) + A_3 e^{-B_3(s/s_0)^\mu t} + A_4 e^{-B_4(s/s_0)^\mu t}). \quad (19)$$

The parameters $A_1, A_2, A_3, A_4, B_1, B_2, B_3, B_4, \alpha, \eta, \mu, m$, and n are free parameters, determined through fitting the data at all the energies. The parameter t_0 is a reference momentum scale (in GeV^2) controlling the onset of the saturation term. However, the first term contains a power law factor t^{-m} which suppresses the cross section at high t

values. And the second exponential term contains a power law factor t^{-n} and a logarithmic correction $\text{Log}(1 + \alpha t/t_0)$. The logarithmic factor grows slowly and enhances the behavior of the cross section mildly as t increases. At small t , $\text{Log}(1 + \alpha t/t_0) \approx \alpha t/t_0$ and it behaves linearly, i.e., the whole correction $\approx t^{-(n-1)}$. At large t , the logarithm grows slowly thereby adding a soft enhancement to the suppression. The fitted parameter values of this model are given in table 6.

7. Model 7

This exponential model with stretched exponential and power-law-type factors is given in the following form

$$\frac{d\sigma(s,t)}{dt} = \sum_{i=1}^p (A_i(s,t) e^{-B_i(s,t)}) e^{-\gamma(t/t_0)^m} (1 + t/t_0)^{-n}. \quad (20)$$

with $i = 1, 2, \dots, p$ and $p = 4$. We obtain the following form of this model by expanding it upto four terms.

$$\frac{d\sigma(s,t)}{dt} = (A_1(s,t) e^{-B_1(s,t)} + A_2(s,t) e^{-B_2(s,t)} + A_3(s,t) e^{-B_3(s,t)} + A_4(s,t) e^{-B_4(s,t)^\mu t}) e^{-\gamma(t/t_0)^m} (1 + t/t_0)^{-n}. \quad (21)$$

Here $A_1(s,t)$, $A_2(s,t)$, $A_3(s,t)$, $A_4(s,t)$, $B_1(s,t)$, $B_2(s,t)$, $B_3(s,t)$, and $B_4(s,t)$ are functions of s and t . These functions are $A_1(s,t) = A_1(s)t^0$, $A_2(s,t) = A_2(s)t^0$, $A_3(s,t) = A_3(s)t^0$, and $A_4(s,t) = A_4(s)t^0$. And $B_1(s,t) = B_1(s)t$, $B_2(s,t) = B_2(s)t$, $B_3(s,t) = B_3(s)t$, and $B_4(s,t) = B_4(s)t$. The $A(s)$ parameters are $A_1(s) = A_1(s/s_0)^\eta$, $A_2(s) = A_2(s/s_0)^\eta$, $A_3(s) = A_3(s/s_0)^\eta$ and $A_4(s) = A_4(s/s_0)^\eta$. The $B(s)$ parameters are $B_1(s) = B_1(s/s_0)^\mu$, $B_2(s) = B_2(s/s_0)^\mu$, $B_3(s) = B_3(s/s_0)^\mu$ and $B_4(s) = B_4(s/s_0)^\mu$. After substituting the values of $A(s)$ and the $A(s)$ parameters, we obtain the following form of this model for fitting.

$$\frac{d\sigma(s,t)}{dt} = (s/s_0)^\eta (A_1 e^{-B_1(s/s_0)^\mu t} + A_2 e^{-B_2(s/s_0)^\mu t} + A_3 e^{-B_3(s/s_0)^\mu t} + A_4 e^{-B_4(s/s_0)^\mu t}) e^{-\gamma(t/t_0)^m} (1 + t/t_0)^{-n}. \quad (22)$$

Here $A_1, A_2, A_3, A_4, B_1, B_2, B_3, B_4, \eta, \mu, \gamma, m$, and n are free parameters, determined through fitting with the data at all the energies. The parameter t_0 is a reference momentum scale (in GeV^2). In this model each term is multiplied with two factors, $e^{-\gamma(t/t_0)^m}$, a stretched exponential and $(1 + t/t_0)^{-n}$, a power-law-type decay factor. Transition between exponential regime at low t and power-law-like regime is made smoothed by these factors. Multiplying $e^{-\gamma(t/t_0)^m}$ with every term modifies the slope beyond a certain range. If $m = 2$ then it can act like a Gaussian suppression. If $m < 1$ then it may decay slower than exponential. If γ is large then stronger suppression occurs in mid-to-high t . The power-law-like factor $(1 + t/t_0)^{-n}$ gives additional control over the tail behavior at high t . For $t \gg t_0$, $(1 + t/t_0)^{-n} \approx (t/t_0)^{-n}$ which provides high momentum suppression. The values of all the parameters of this model are given in Table 7.

These proposed models are used to calculate the total elastic and inelastic cross sections as discussed in detail in section III. Chi-square is calculated to determine the accuracy of the models. Absolute relative error (ARE) is calculated for total elastic cross section. The calculated values of σ_{el} , σ_{tot} , and σ_{inel} are compared with other's work and the best models which predicted the most accurate values are identified.

III. RESULTS AND DISCUSSION

In this study, we performed a systematic fitting of elastic differential cross-section data for pp scattering over a wide range of energies, including both GeV and TeV scales, using seven distinct composite exponential models. Each model is designed to capture different kinematic features of the data, reflecting the complex internal structure of the proton and the energy-dependent nature of elastic scattering. Here, we discuss the results with emphasis on the possible physical insights extracted from the fitting behavior of our models with the data. The models are fitted to the elastic scattering data collected at various center-of-mass energies, from GeV energies of 23, 23.5, 27.43, 30.7, 44.7, 52.8, and 62.5 GeV to LHC energies of 2.76, 7, 8, 13 TeV. And at extrapolated values at 200 and 800 GeV, and 14, 15, and 28 TeV. The results of the obtained fits are shown in Figures 1-7.

In most fits of our models, the chi-square per degree of freedom (χ^2) values are reasonably small that indicates good

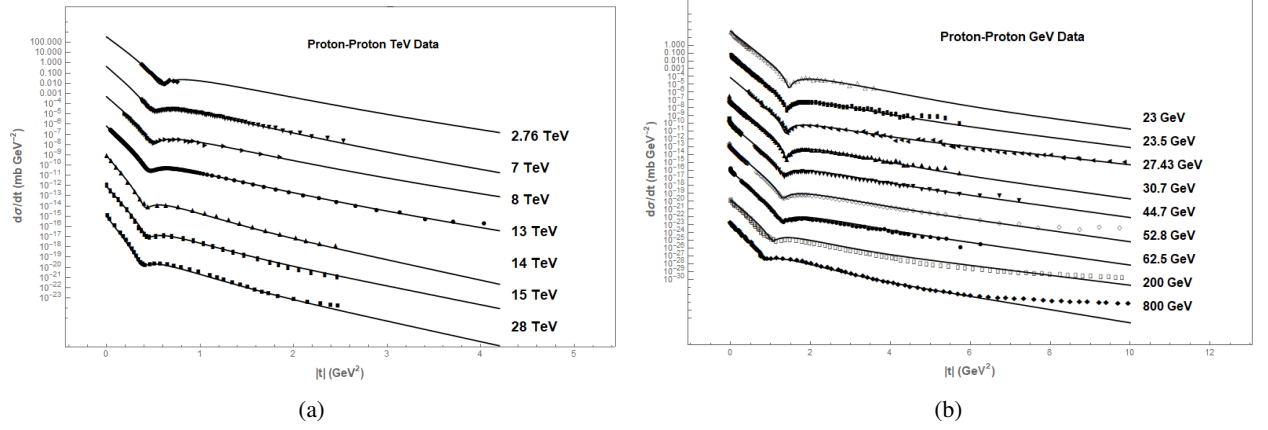


FIG. 1: (a) Model 1 fits on the pp elastic differential cross section data in the energy range $2.76 \leq \sqrt{s} \leq 28 \text{ TeV}$. Filled squares represent data points taken from extrapolated data at 28 TeV, filled rectangles represent data points taken from extrapolated data at 15 TeV, filled up triangles represent data points taken from extrapolated data at 14 TeV, filled circles represent the data at 13 TeV, filled right triangles represent the data at 8 TeV, filled down triangles represent the data 7 TeV, and filled diamonds represent the data at 2.76 TeV. Data and model values are multiplied by $10^{-3(n-1)}$, where n is the number of curve and corresponding data set starting from top. Solid line represents the fit by our model on the data. (b) Model 1 fits on the pp elastic scattering data of differential cross section in the energy range $23 \leq \sqrt{s} \leq 800 \text{ GeV}$. Filled diamonds represent data points taken from extrapolated data at 800 GeV, empty rectangles represent the data at 200 GeV, filled circles represent data at 62.5 GeV, empty diamonds represent the data at 52.8 GeV, filled down triangles represent the data at 44.7 GeV, filled up triangles represent the data at 30.7 GeV, filled left triangles represent the data at 27.43 GeV, filled solid rectangles represent the data at 23.5 GeV, and empty up triangles represent the data at 23 GeV. Data and model values are multiplied by $10^{-3(n-1)}$, where n is the number of curve and corresponding dataset starting from top. Solid line represents the fit by our model on the data.

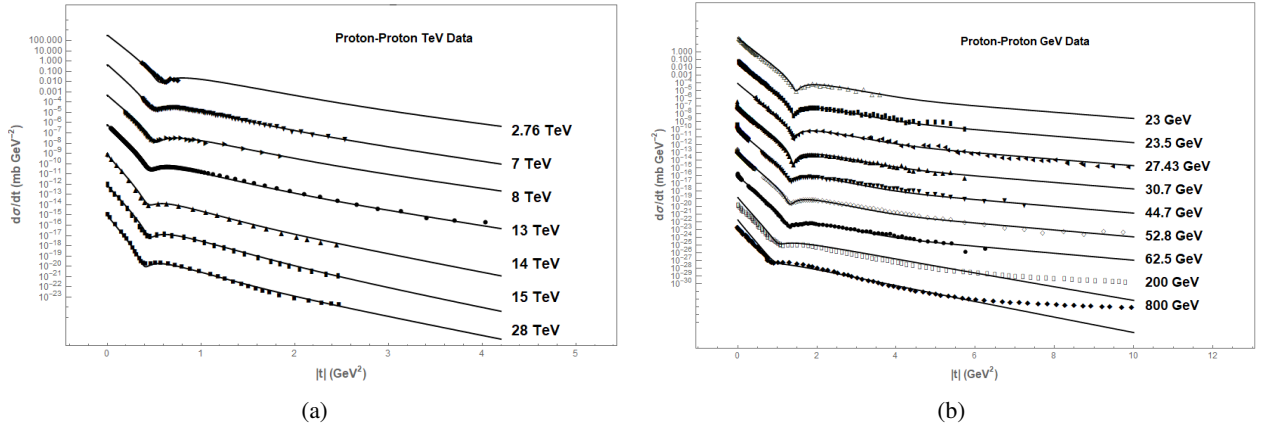


FIG. 2: (a) Same legend as in Fig.1 with Model 2. (b) Same legend as in Fig.1 with Model 2.

fitting agreement of our models with the data. We have used the following expression for dimensionless χ^2 .

$$\chi^2 = \frac{\sum_{i=1}^N [(d\sigma/dt)_i^{\text{model}} - (d\sigma/dt)_i^{\text{data}}]^2}{\sum_{i=1}^N [(d\sigma/dt)_i^{\text{data}}]^2} \quad (23)$$

with $i = 1, 2, 3, \dots, N$, number of data points. It is a normalized error measure which is particularly useful to determine goodness of fit when experimental uncertainties are not known. The χ^2 values for each model across all the energies along with the fitted parameter values are given in the Tables 1-7. In some cases especially for 200 GeV and 800 GeV data, physical shape of the data and the optimal parameter values for total elastic cross section are prioritized, which

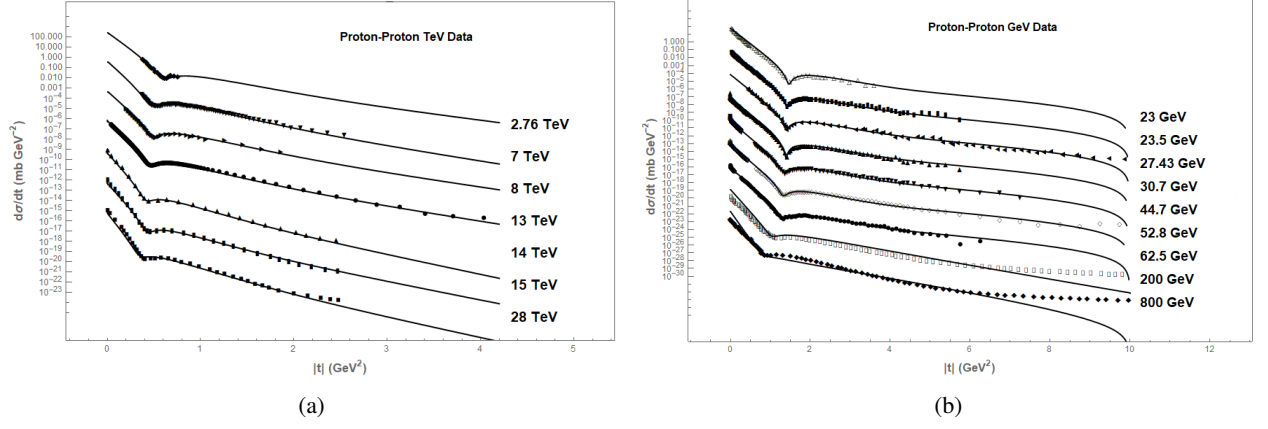


FIG. 3: (a) Same legend as in Fig.1 with Model 3. (b) Same legend as in Fig.1 with Model 3.

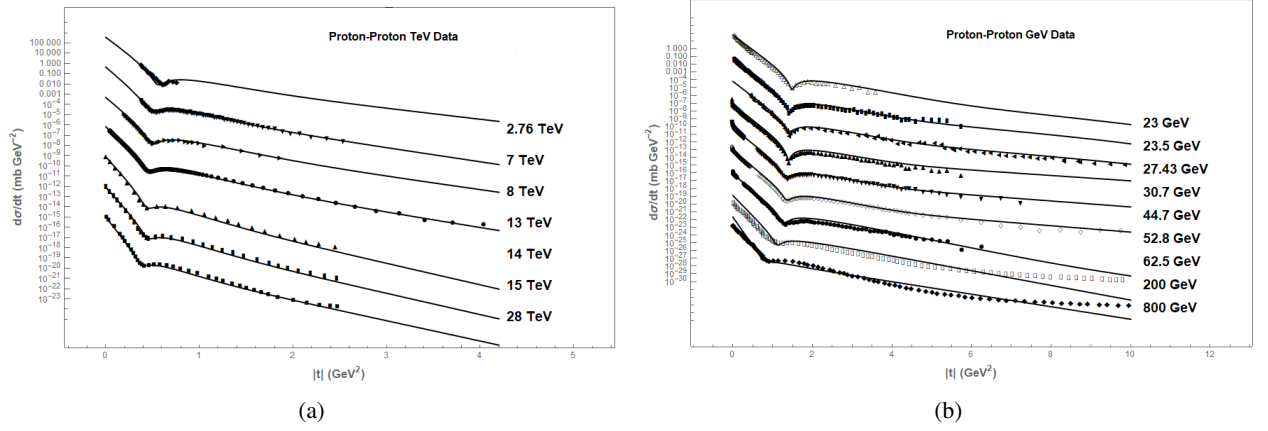


FIG. 4: (a) Same legend as in Fig.1 with Model 4. (b) Same legend as in Fig.1 with Model 4.

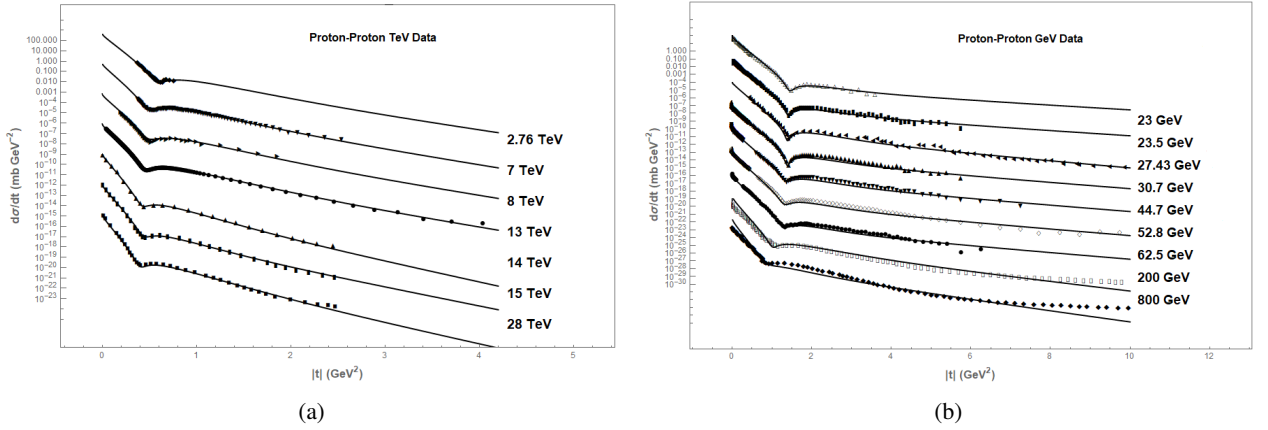


FIG. 5: (a) Same legend as in Fig.1 with Model 5. (b) Same legend as in Fig.1 with Model 5.

are critical for physical interpretation, even if chi-square values are large.

From Tables (1-7), it is observed that χ^2 for the model 1 lies in range ($0.00029 \leq \chi^2 \leq 85.2839$), for the model 2 lies in range ($0.0000844489 \leq \chi^2 \leq 66.1178$), for the model 3 lies in range ($0.000111596 \leq \chi^2 \leq 85.0032$), for the model 4 lies in range ($0.000025363 \leq \chi^2 \leq 86.8693$), for the model 5 lies in range ($0.00316228 \leq \chi^2 \leq 116.463$), for the

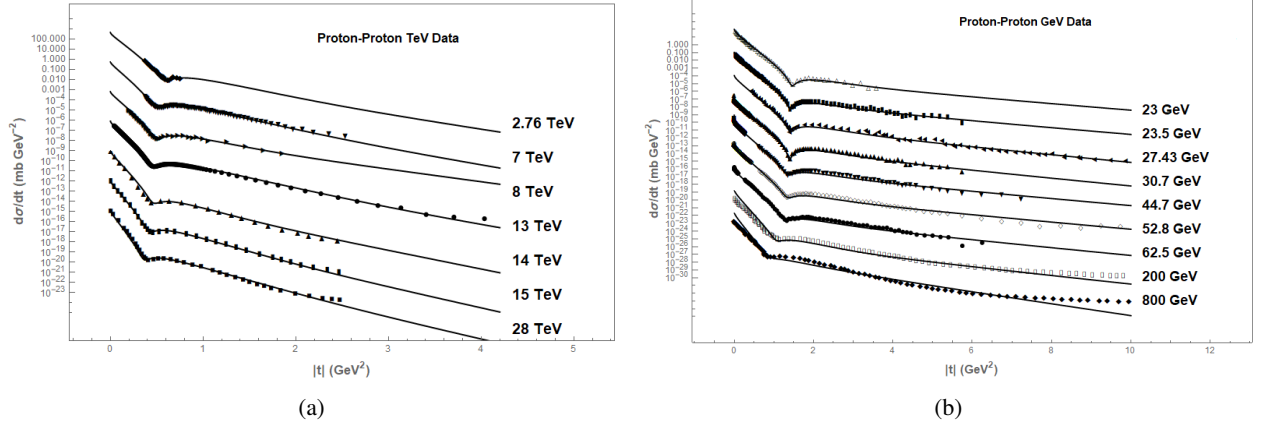


FIG. 6: (a) Same legend as in Fig.1 with Model 6. (b) Same legend as in Fig.1 with Model 6.

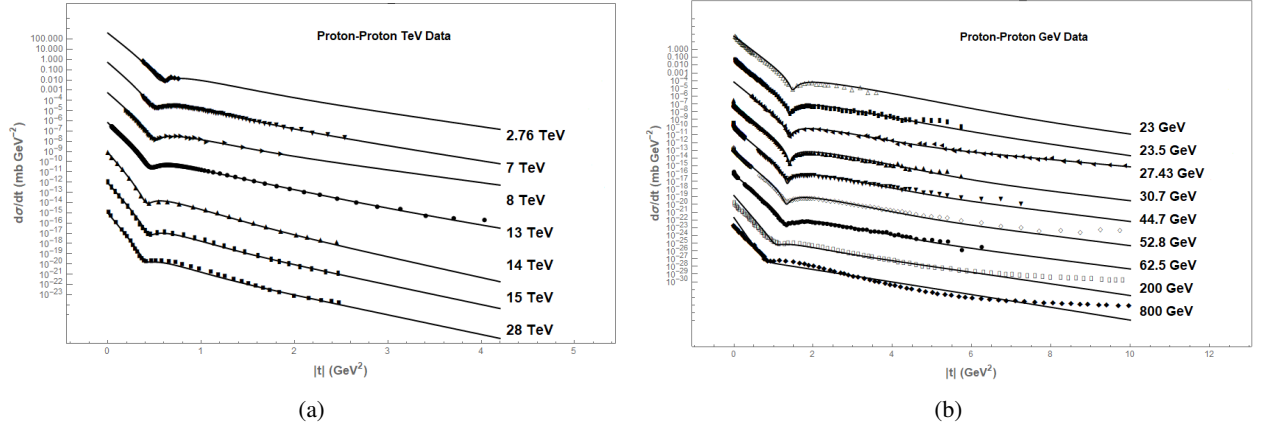


FIG. 7: (a) Same legend as in Fig.1 with Model 7. (b) Same legend as in Fig.1 with Model 7.

model 6 lies in range $(0.00217907 \leq \chi^2 \leq 111.098)$, and for the model 7 lies in range $(0.0000822846 \leq \chi^2 \leq 86.4296)$. From this observation, it is concluded that model 2 is best with respect to least value of χ^2 .

Our models contained fewer parameters as compared to the other earlier fits on the ISR and TOTEM data. A lesser number of parameters allows better modeling of the elastic differential cross section to obtain empirical information from the data. Fewer parameters reduce the chance of fitting noise or fluctuations in the data. Models with lesser parameters are very suitable in model-independent or phenomenological approaches, where the goal is to extract stable physical patterns from the experimental data. Such models are also used due to better stability when extrapolated beyond the range of current data to higher energies. With fewer parameter models, numerical fitting algorithms converge more quickly, computational efficiency is often improved, and estimation of uncertainties becomes straightforward.

The differential cross-section fits of our models exhibited several important features across broad energy ranges. At small $|t|$, the cross-section is dominated by a steep exponential fall-off. This region probes the large-distance or peripheral structure of the proton. As energy increases, the slope parameter B of the forward exponential becomes larger, a phenomenon known as the "shrinkage of the forward peak" as mentioned in refs. [9] [11]. The shrinkage is also explained by Regge phenomenology in ref. [65] and suggests that the proton becomes more transparent with increase in energy and its effective size increases. This indicates that the effective radius of interaction of the proton increases with center-of-mass energy. The shrinkage is often utilized to produce the slopes of effective trajectories in various elastic scattering phenomena. It is also important to study this phenomenon as it gives information about many observables, for instance, because of this phenomenon the elastic cross-section becomes a decreasing fraction of the total cross-section as $\log(s) \rightarrow \infty$.

A prominent dip followed by a bump emerges at intermediate $|t|$ values around $|t|$ range $(0.5\text{--}2.0 \text{ GeV}^2)$, especially visible at the data at GeV energies and around $|t|$ range $(0.1\text{--}0.4 \text{ GeV}^2)$ at the data at TeV energies. The position

TABLE I: Parameter values of the Model 1.

\sqrt{s}	A_1	A_2	A_3	A_4	B_1	B_2	B_3	B_4	η	μ	χ^2
	(mb/GeV ²)	(mb/GeV ²)	(mb/GeV ²)	(mb/GeV ²)	(GeV ⁻²)	(GeV ⁻²)	(GeV ⁻²)	(GeV ⁻²)			
23 GeV	20.7284	5×10^{-5}	-0.06	0.04	9.20	1.59	3.00	2.754	0.17	1×10^{-5}	0.03080
23.5 GeV	24.3006	1×10^{-4}	-0.06	0.04	9.44	1.50	3.00	2.754	0.1506	2×10^{-4}	0.01296
27.43 GeV	25.9808	1×10^{-4}	-0.06	0.04	9.57	1.29	3.00	2.754	0.1503	0.004	0.04859
30.7 GeV	25.944	1×10^{-4}	-0.06	0.04	9.48	1.59	3.00	2.754	0.1503	0.005	0.52595
44.7 GeV	22.492	3×10^{-4}	-0.06	0.04	9.65	1.59	3.00	2.754	0.152	0.003	0.58087
52.8 GeV	22.1529	3×10^{-4}	-0.06	0.04	9.67	1.59	3.00	2.754	0.1503	0.005	0.43732
62.5 GeV	22.000	3×10^{-4}	-0.06	0.04	9.67	1.59	3.00	2.754	0.1503	0.005	0.26881
200 GeV	102.68321	1×10^{-4}	-0.06	0.01	8.65	1.00	3.00	2.00	0.025	0.04	36.9703
800 GeV	120.68321	1×10^{-4}	-0.06	0.01	8.50	1.00	3.00	2.00	0.038	0.05	85.2839
2.76 TeV	234.327	1.305	-9.06	0.04	15.15	4.40	7.207	3.10	0.200	1×10^{-4}	0.01324
7 TeV	292.000	1.305	-9.06	0.04	15.50	4.30	7.207	3.10	0.103	0.034	0.00345
8 TeV	320	1.305	-9.06	0.04	15.95	4.20	7.207	2.925	0.105	0.025	0.00269
13 TeV	375.432	1.305	-9.06	0.04	16.50	4.10	7.207	2.894	0.103	0.034	0.00029
14 TeV	670.487	1.305	-9.06	0.04	16.20	4.60	7.207	3.00	0.04	0.08	0.0281741
15 TeV	675.758	1.305	-9.06	0.04	16.00	4.60	7.207	2.894	0.035	0.07	0.09265
28 TeV	695.734	1.305	-9.06	0.04	16.70	4.40	7.207	2.894	0.05	0.07	0.06351

TABLE II: Parameter values of the Model 2.

\sqrt{s}	A_1	A_2	A_3	A_4	B_1	C_1	B_2	B_3	B_4	α	m	η	μ	χ^2
	(mb/GeV ²)	(mb/GeV ²)	(mb/GeV ²)	(mb/GeV ^{2(1-m)})	(GeV ⁻²)	(GeV ⁻²)	(GeV ⁻²)	(GeV ⁻²)	(GeV ⁻²)					
23 GeV	20.420	1×10^{-5}	-0.06	0.02	7.92	5.00	0.83	3.00	2.374	0.18	0.1	0.145	0.018	0.0386587
23.5 GeV	22.022	1×10^{-5}	-0.06	0.02	8.00	5.00	0.83	3.00	2.374	0.18	0.1	0.147	0.023	0.00962473
27.43 GeV	24.751	1×10^{-5}	-0.06	0.02	8.08	5.00	0.83	3.00	2.374	0.18	0.1	0.146	0.022	0.0179198
30.7 GeV	22.200	1×10^{-5}	-0.06	0.02	8.03	5.00	0.83	3.00	2.374	0.18	0.1	0.146	0.022	0.533835
44.7 GeV	22.264	1×10^{-5}	-0.06	0.02	8.00	5.00	0.82	3.00	2.374	0.18	0.1	0.147	0.027	0.536467
52.8 GeV	20.645	1×10^{-5}	-0.06	0.02	8.00	5.00	0.83	3.00	2.374	0.18	0.1	0.147	0.027	0.368381
62.5 GeV	20.694	1×10^{-5}	-0.06	0.02	8.00	5.00	0.83	3.00	2.374	0.18	0.1	0.147	0.027	0.190087
200 GeV	108.683	0.01	-0.06	0.01	10.90	5.50	3.70	3.00	1.60	0.18	0.8	0.008	0.018	38.7873
800 GeV	132.683	0.01	-0.06	0.02	10.0	5.00	3.00	3.00	1.60	0.18	0.8	0.008	0.024	66.1178
2.76 TeV	220.870	1.20	-9.06	0.04	15.250	5.80	4.35	7.207	2.454	0.2	1.00	0.150	0.001	0.085954
7 TeV	225.000	1.20	-9.06	0.04	15.02	4.00	4.45	7.207	2.454	0.2	1.00	0.1503	0.042	0.00376058
8 TeV	162.996	1.10	-9.06	0.04	15.25	5.70	4.40	7.50	2.55	0.5	1.00	0.17	0.015	0.000189877
13 TeV	251.513	1.20	-9.06	0.04	15.272	4.00	4.35	7.207	2.454	0.2	1.00	0.1503	0.045	0.0000844489
14 TeV	510.123	1.20	-9.06	0.04	15.70	4.00	4.70	7.207	2.654	0.2	1.00	0.043	0.07	0.0453653
15 TeV	535.025	1.20	-9.06	0.04	16.0	4.00	4.60	7.207	2.954	0.2	1.00	0.04	0.06	0.0977654
28 TeV	560.250	1.20	-9.06	0.04	16.50	5.00	4.55	7.207	2.654	0.2	1.00	0.0503	0.06	0.0683303

of the dip shifts towards smaller $|t|$ values with increasing energy, indicating that the coherent interference between elastic amplitudes becomes more prominent at larger impact [9][61]. At large $|t|$ values, the cross-section falls more slowly. This hard tail reflects deep elastic scattering between valence quarks, revealing the short-distance dynamics of the proton. Properly modeling this region requires either a modified exponential or a power-law behavior in the fit. Near the very small $|t|$ regime ($t \rightarrow 0$), the cross-section tends to level off due to the finite proton size and effects of Coulomb-nuclear interference. Careful fitting in this region is crucial to accurately extract the total cross section via extrapolation. Our models adopt these features to varying degrees depending on how many exponential terms and corrections are included. The outer region composed of soft $q\bar{q}$ condensate cloud is probed at very small $|t|$ values. The middle region or baryonic shell influences the intermediate $|t|$ behavior where the dip appears. The core region composed of valence quarks is involved at large $|t|$ through hard scattering processes. Thus, the evolution of the shape of $\frac{d\sigma}{d|t|}$ with energy directly reflects the changing role of different components of proton with increasing center-of-mass energy.

TABLE III: Parameter values of the Model 3.

\sqrt{s}	A_1	A_2	A_3	A_4	B_1	B_2	B_3	B_4	α	m	η	μ	χ^2
	(mb/GeV ²)	(mb/GeV ²)	(mb/GeV ²)	(mb/GeV ^{2(1-m)})	(GeV ⁻²)	(GeV ⁻²)	(GeV ⁻²)	(GeV ⁻²)					
23 GeV	24.000	1×10^{-5}	-0.06	0.02	8.03	0.53	3.00	2.374	0.1	0.1	0.145	0.018	0.0310974
23.5 GeV	24.618	1×10^{-5}	-0.06	0.02	8.075	0.53	3.00	2.374	0.1	0.1	0.147	0.023	0.0140383
27.43 GeV	26.5304	1×10^{-5}	-0.06	0.02	8.13	0.53	3.00	2.374	0.1	0.1	0.146	0.023	0.0176169
30.7 GeV	24.805	1×10^{-5}	-0.06	0.02	8.11	0.53	3.00	2.374	0.1	0.1	0.146	0.023	0.55424
44.7 GeV	23.682	1×10^{-5}	-0.06	0.02	8.00	0.53	3.00	2.374	0.1	0.1	0.147	0.027	0.57592
52.8 GeV	22.539	1×10^{-5}	-0.06	0.02	8.00	0.53	3.00	2.374	0.1	0.1	0.147	0.027	0.441208
62.5 GeV	23.0986	1×10^{-5}	-0.06	0.02	8.00	0.53	3.00	2.374	0.1	0.1	0.147	0.027	0.258126
200 GeV	108.683	0.01	-0.06	0.01	10.90	3.70	3.00	1.60	0.1	0.8	0.018	0.018	35.7519
800 GeV	120.000	0.001	-0.06	0.01	8.50	0.90	3.00	2.00	0.1	0.8	0.038	0.05	85.0032
2.76 TeV	225.036	1.20	-9.06	0.04	14.000	4.350	7.207	2.454	0.1	1.0	0.150	0.001	0.00102214
7 TeV	250.000	1.20	-9.06	0.04	15.10	4.10	7.207	2.754	0.1	1.0	0.1503	0.04	0.0475413
8 TeV	270.209	1.20	-9.06	0.04	16.40	4.30	7.50	2.55	0.1	1.0	0.1603	0.028	0.0142995
13 TeV	299.1	1.20	-9.06	0.04	15.733	4.160	7.207	2.454	0.1	1.0	0.1503	0.045	0.000111596
14 TeV	400.958	1.200	-9.06	0.04	16.0	4.70	7.50	2.90	0.1	1.0	0.020	0.070	0.292235
15 TeV	415.373	1.200	-9.06	0.04	16.20	4.70	7.50	2.80	0.1	1.0	0.02	0.062	0.355332
28 TeV	490.411	1.20	-9.06	0.04	17.10	4.20	7.50	2.80	0.1	1.0	0.022	0.065	0.311984

TABLE IV: Parameter values of the Model 4.

\sqrt{s}	A_1	A_2	A_3	A_4	B_1	B_2	B_3	B_4	α	β	t_0	η	μ	χ^2
	(mb/GeV ²)	(mb/GeV ²)	(mb/GeV ²)	(mb/GeV ²)	(GeV ⁻²)	(GeV ⁻²)	(GeV ⁻²)	(GeV ⁻²)			(GeV ²)			
23 GeV	24.946	1×10^{-5}	-0.06	0.02	8.12	0.90	3.00	2.364	0.1	0.07	1.0	0.136	0.007	0.032293
23.5 GeV	24.316	1×10^{-5}	-0.06	0.02	8.125	0.68	3.00	2.364	0.1	0.08	1.0	0.146	0.015	0.0161873
27.43 GeV	24.315	1×10^{-5}	-0.06	0.02	8.05	0.68	3.00	2.364	0.1	0.07	1.0	0.146	0.014	0.0199193
30.7 GeV	23.646	1×10^{-5}	-0.06	0.02	8.12	0.68	3.00	2.364	0.1	0.02	1.0	0.146	0.014	0.571993
44.7 GeV	23.289	1×10^{-5}	-0.06	0.02	8.00	0.72	3.00	2.372	0.1	0.02	1.0	0.1402	0.020	0.600485
52.8 GeV	22.817	1×10^{-5}	-0.06	0.02	8.00	0.68	3.00	2.364	0.1	0.02	1.0	0.1407	0.018	0.457901
62.5 GeV	23.324	1×10^{-5}	-0.06	0.02	8.0	0.68	3.0	2.364	0.1	0.02	1.0	0.1407	0.020	0.279219
200 GeV	101.683	0.01	-0.06	0.01	9.80	3.70	3.00	1.80	0.1	0.002	1.0	0.018	0.018	32.5794
800 GeV	122.000	0.001	-0.06	0.01	8.50	0.950	3.00	2.00	0.1	0.002	1.0	0.038	0.05	86.8693
2.76 TeV	225.316	1.20	-9.06	0.04	15.210	4.05	7.407	2.454	0.1	0.2	1.0	0.250	3×10^{-4}	0.0438426
7 TeV	235.999	1.20	-9.06	0.04	14.40	4.075	7.207	2.60	0.1	0.2	1.0	0.1703	0.05	0.0153044
8 TeV	262.409	1.20	-9.06	0.04	15.85	4.00	7.50	2.75	0.1	0.2	1.0	0.1503	0.02	0.000651172
13 TeV	313.521	1.20	-9.06	0.04	15.70	3.75	7.207	2.654	0.1	0.2	1.0	0.1503	0.05	0.000025363
14 TeV	525.994	1.20	-9.06	0.04	14.82	4.450	7.207	3.10	0.1	0.2	1.0	0.074	0.084	0.0445362
15 TeV	550.376	1.20	-9.06	0.04	14.85	4.450	7.207	3.10	0.1	0.2	1.0	0.075	0.08	0.0884937
28 TeV	570.456	1.20	-9.06	0.04	15.30	4.250	7.207	2.684	0.1	0.2	1.0	0.08	0.08	0.0618852

A. Comparison with Other Models

At the extrapolated energies of $\sqrt{s} = 14, 15$, and 28 TeV which is beyond the capabilities of LHC, the results of fitting of our models shows good agreement with the differential cross sections fits calculated by extended Bialas-Bzdak (BB) model of ref. [47]. The BB model treats the proton as a composite object with a real part in the scattering amplitude satisfying unitarity, offers predictions that are sensitive to the spatial configuration within the proton. Our models successfully fitted both the diffractive cone and the first diffractive minimum regions, mirroring the non-trivial, non-exponential features in the differential cross-section as predicted by their approach. In our models the presence of multiple exponential terms with varying weights and slopes are responsible for producing the interference patterns and diffractive features related to the predictions of the BB model formalism at the extrapolated LHC energies. At the 27.43 GeV data, our models showed good fitting agreement with the fitting result of the Froissaron and Maximal Odderon (FMO) model of ref. [63] which stems from analyticity, crossing symmetry, and unitarity constraints, introduces asymptotically growing even-under-crossing and odd-under-crossing components in the amplitude. This model employed simplifying assumptions to study the role of Froissaron and Maximal Odderon in spin phenomena during elastic scattering. The FMO model holds the Froissaron responsible for the rise in the total cross section and the Max-

TABLE V: Parameter values of the Model 5.

\sqrt{s}	A_1	A_2	A_3	A_4	B_1	B_2	B_3	B_4	m	n	p	t_0	η	μ	χ^2
	(mb/GeV ^{2(1-m)})	(mb/GeV ²⁽¹⁻ⁿ⁾)	(mb/GeV ²)	(mb/GeV ²)	(GeV ⁻²)	(GeV ⁻²)	(GeV ⁻²)	(GeV ⁻²)				(GeV ²)			
23 GeV	24.939	1×10^{-4}	-0.06	0.01	7.305	0.45	3.0	2.2	0.15	1.30	0.3	10	0.06	0.034	0.0412167
23.5 GeV	24.309	1×10^{-4}	-0.06	0.01	7.32	0.49	3.0	2.19	0.2	1.34	0.3	10	0.05	0.037	0.0127373
27.43 GeV	32.7578	1×10^{-4}	-0.06	0.01	7.40	0.69	3.00	2.20	0.10	1.30	0.3	10	0.08	0.042	0.0971615
30.7 GeV	40.2425	1×10^{-4}	-0.06	0.01	7.475	0.59	3.0	2.216	0.20	1.30	0.3	10	0.005	0.042	0.169058
44.7 GeV	28.0184	1×10^{-4}	-0.06	0.01	7.26	0.59	3.0	2.190	0.20	1.34	0.3	10	0.05	0.04	0.212259
52.8 GeV	26.5816	1×10^{-4}	-0.06	0.01	7.23	0.59	3.0	2.190	0.20	1.34	0.3	10	0.05	0.042	0.0963651
62.5 GeV	25.7203	1×10^{-4}	-0.06	0.01	7.22	0.59	3.0	2.190	0.20	1.34	0.3	10	0.05	0.042	0.0179891
200 GeV	67.000	0.001	-0.06	0.01	9.70	0.97	3.0	2.0	0.20	1.34	0.3	10	0.0005	0.026	42.3886
800 GeV	87.000	0.001	-0.06	0.01	8.40	0.88	3.00	2.00	0.20	1.34	0.3	10	0.0005	0.04	116.463
2.76 TeV	180.000	0.99	-9.06	0.04	13.67	4.2	7.07	2.854	0.1	0.01	0.1	20	0.15	0.043	0.0565908
7 TeV	175.000	0.99	-9.06	0.04	14.30	4.2	7.307	2.854	0.1	0.01	0.1	20	0.15	0.045	0.00395242
8 TeV	187.000	1.3	-9.06	0.04	14.20	4.05	6.77	2.754	0.1	0.01	0.1	20	0.15	0.050	0.0332063
13 TeV	195.670	1.3	-9.06	0.04	14.4527	4.0	6.82	2.754	0.1	0.01	0.1	20	0.15	0.045	0.00316228
14 TeV	480.056	1.0	-9.06	0.04	19.40	5.40	9.10	3.82	0.1	0.01	0.1	20	0.012	0.036	0.0244666
15 TeV	510.723	1.1	-9.04	0.04	21.00	6.0	9.80	3.9	0.1	0.01	0.1	20	0.12	0.015	0.057712
28 TeV	550.817	1.1	-9.04	0.04	22.10	5.70	9.80	4.200	0.1	0.01	0.1	20	0.02	0.015	0.0568453

TABLE VI: Parameter values of the Model 6.

\sqrt{s}	A_1	A_2	A_3	A_4	B_1	B_2	B_3	B_4	m	n	α	t_0	η	μ	χ^2
	(mb/GeV ^{2(1-m)})	(mb/GeV ²⁽¹⁻ⁿ⁾)	(mb/GeV ²)	(mb/GeV ²)	(GeV ⁻²)	(GeV ⁻²)	(GeV ⁻²)	(GeV ⁻²)				(GeV ²)			
23 GeV	23.215	1×10^{-4}	-0.06	0.01	7.172	0.69	3.00	2.190	0.20	1.34	2.7	1.0	0.05	0.035	0.0335962
23.5 GeV	24.4095	1×10^{-4}	-0.06	0.01	7.210	0.69	3.00	2.190	0.20	1.34	2.7	1.0	0.05	0.04	0.012264
27.43 GeV	28.014	1×10^{-4}	-0.06	0.01	7.210	0.79	3.00	2.190	0.20	1.34	2.7	1.0	0.05	0.04	0.144866
30.7 GeV	29.369	1×10^{-4}	-0.06	0.01	7.30	0.79	3.00	2.190	0.20	1.34	2.7	1.0	0.05	0.04	0.17382
44.7 GeV	28.0497	1×10^{-4}	-0.06	0.01	7.20	0.69	3.00	2.190	0.20	1.34	2.7	1.0	0.05	0.04	0.216039
52.8 GeV	26.5437	1×10^{-4}	-0.06	0.01	7.15	0.69	3.00	2.190	0.20	1.34	2.7	1.0	0.05	0.04	0.0998485
62.5 GeV	25.736	1×10^{-4}	-0.06	0.01	6.70	0.60	3.00	2.290	0.20	1.34	2.7	1.0	0.05	0.05	0.0191549
200 GeV	60.000	0.0001	-0.06	0.01	8.22	0.76	3.00	2.00	0.20	1.34	2.40	1.0	0.01	0.04	41.8613
800 GeV	75.000	0.001	-0.06	0.01	8.22	0.96	3.0	2.0	0.20	1.34	2.4	1.0	0.01	0.04	111.098
2.76 TeV	180.341	1.30	-9.06	0.04	13.620	4.75	7.205	2.954	0.1	0.01	2.7	1.0	0.1503	0.045	0.0741255
7 TeV	185.545	1.30	-9.06	0.04	13.90	4.45	7.205	2.954	0.1	0.01	2.7	1.0	0.1303	0.05	0.00405363
8 TeV	187.374	1.30	-9.06	0.04	14.00	4.58	7.255	2.354	0.1	0.01	2.7	1.0	0.1503	0.045	0.00453365
13 TeV	198.941	1.30	-9.06	0.04	14.489	4.15	7.205	2.854	0.1	0.01	2.7	1.0	0.1503	0.045	0.00217907
14 TeV	415.000	1.10	-9.04	0.04	19.30	6.20	9.80	3.80	0.1	0.01	2.7	1.0	0.030	0.020	0.0337606
15 TeV	475.146	1.10	-9.04	0.04	19.90	5.80	9.80	4.00	0.1	0.01	2.7	1.0	0.031	0.030	0.0497802
28 TeV	535.623	1.10	-9.04	0.04	21.00	5.20	9.80	3.80	0.1	0.01	2.7	1.0	0.031	0.034	0.0537888

imal Odderon contribution occurs with a distinct behavior in the real part of the amplitude. Though our models may not explicitly separate odd and even components, the successful fit of our models to the data where Odderon effects are most visible implying that the superposition of exponential forms can accommodate such subtleties indirectly through effective combinations of parameters. At 200 GeV and 800 GeV, our models showed a strong agreement with the predicted differential cross section fit results by the improved impact picture framework of ref. [62]. This framework incorporates a refined matter distribution tied to the charge distribution of proton, Regge background contributions, and a non-trivial hadronic matter current. The impact picture model refines the matter distribution by tying it to the known electromagnetic charge distribution of the proton, accounts for the spatial overlap and opacity function in the transverse impact parameter space. The use of multiple exponentials in our models allows for an approximate inverse Fourier representation of complex impact parameter distributions. The accurate reproduction of the differential cross-section data particularly the forward peak, dip structure, and low- $|t|$ behavior confirms that the fitting by our models can accurately encapsulate the underlying dynamics of proton. The close correspondence of our fitting results with these approaches, both at lower ISR energies, higher LHC energies and at extrapolated energies, confirms the physical relevance of the our multi-component exponential structures as models of the elastic differential cross section. This agreement implies that the models used in this study are not merely phenomenological tools with lesser parameters but encapsulate the key physical mechanisms underlying proton elastic interactions, such as diffraction dominance

TABLE VII: Parameter values of the Model 7.

\sqrt{s}	A_1	A_2	A_3	A_4	B_1	B_2	B_3	B_4	γ	m	t_0	n	η	μ	χ^2
	(mb/GeV ²)	(mb/GeV ²)	(mb/GeV ²)	(mb/GeV ²)	(GeV ⁻²)	(GeV ⁻²)	(GeV ⁻²)	(GeV ⁻²)			(GeV ²)				
23 GeV	22.240	3×10^{-5}	-0.06	0.04	9.170	1.79	3.00	2.754	0.001	1.1	20	5.5	0.1503	0.0002	0.0427891
23.5 GeV	24.389	1×10^{-4}	-0.06	0.04	9.370	1.79	3.00	2.754	0.001	1.1	20	5.5	0.1503	0.006	0.0127953
27.43 GeV	24.968	1×10^{-5}	-0.06	0.04	9.250	1.20	3.00	2.754	0.001	1.1	20	5.5	0.1503	0.009	0.0268167
30.7 GeV	24.999	1×10^{-5}	-0.06	0.04	9.260	1.50	3.00	2.754	0.001	1.1	20	5.5	0.1503	0.009	0.540173
44.7 GeV	23.464	3×10^{-5}	-0.06	0.04	9.250	1.50	3.00	2.754	0.001	1.1	20	5.5	0.1503	0.012	0.570122
52.8 GeV	22.771	3×10^{-5}	-0.06	0.04	9.20	1.50	3.00	2.754	0.001	1.1	20	5.5	0.1503	0.014	0.424917
62.5 GeV	22.789	3×10^{-5}	-0.06	0.04	9.18	1.50	3.00	2.754	0.001	1.1	20	5.5	0.1503	0.014	0.251273
200 GeV	102.00	0.0003	-0.06	0.04	10.20	1.40	3.00	2.754	0.001	1.1	20	5.5	0.032	0.03	41.9187
800 GeV	132.000	0.001	-0.06	0.01	4.50	0.55	3.00	2.00	0.001	1.1	20	5.5	0.032	0.1	86.4296
2.76 TeV	293.629	1.30	-9.70	0.04	14.82	4.68	7.35	2.79	0.001	1.1	20	0.1	0.1503	0.045	0.0970069
7 TeV	290.745	1.30	-9.70	0.04	15.0	4.4	7.23	2.79	0.001	1.1	20	0.1	0.1502	0.045	0.0414183
8 TeV	297.261	1.30	-9.06	0.04	15.05	4.3	7.0	2.35	0.001	1.1	20	0.1	0.1503	0.045	0.0000822846
13 TeV	498.282	1.30	-9.06	0.04	16.91	3.80	7.00	2.754	0.001	1.1	20	0.1	0.06	0.044	0.0000930385
14 TeV	590.086	1.20	-9.06	0.04	15.90	4.48	7.207	3.05	0.001	1.1	20	0.1	0.06	0.08	0.0338774
15 TeV	605.075	1.20	-9.06	0.04	15.30	4.70	7.207	2.884	0.001	1.1	20	0.1	0.06	0.08	0.0840861
28 TeV	635.543	1.20	-9.06	0.04	15.20	4.60	7.207	2.684	0.001	1.1	20	0.1	0.06	0.075	0.0626819

at small momentum transfer, the emergence of dips and bumps associated with substructure of proton, and the hard scattering tail at large- $|t|$ at all the available data. The strength of our composite exponential models lies in their phenomenological flexibility.

B. Total Elastic Cross Section

The total elastic cross section σ_{el} is calculated by numerically integrating the differential cross section models with the fitted parameters over all the energies by the following equation.

$$\sigma_{el} = \int_{t_{min}}^{t_{max}} \frac{d\sigma}{dt} dt \quad (24)$$

For all the TeV and GeV energies the $\frac{d\sigma}{dt}$ models are integrated in $|t|$ -range of $0 \leq |t| \leq 4.2 \text{ GeV}^2$ and $0 \leq |t| \leq 12 \text{ GeV}^2$ respectively. The resulting values of σ_{el} which are shown in the Table 8, show good consistency with experimental measurements where available.

Notably, σ_{el} increases with energy, reflecting the growing blackness of the proton. At ISR energies (23 GeV - 62.5 GeV), σ_{el} remains relatively small (~ 7 –10 mb). At LHC energies (2.76 TeV - 13 TeV), σ_{el} rises significantly (~ 25 –30 mb). Extrapolated values at 14, 15, and 28 TeV predict further moderate increases which is consistent with such an increasing trends reported by the TOTEM and COMPETE Collaborations [25][66]. Accurate determination of σ_{el} is critical for understanding various quantities and physical features at ultra-high energies.

An absolute relative error (ARE) estimation of σ_{el} is performed for each model across energy range (23.5 GeV - 13 TeV). The calculated ARE values are mentioned in Table 9. For the relative error we used the following equation.

$$\partial\sigma = \frac{|\sigma_{model} - \sigma_{exp}|}{\sigma_{exp}} \times 100 \quad (25)$$

Where $\partial\sigma$ is the relative percentage absolute error or percentage deviation from the reference value. σ_{model} and σ_{exp} are the model and experimental values of the elastic cross section. The model 1 results of σ_{el} showed the relative error in range of 0.0248985% – 7.82913%. The model 2 results showed the error in range of 0.120472% – 3.1567%. The model 3 results showed the error in range of 0.0952381% – 5.19177%. The model 4 results showed the error in range 0.718533% – 5.22585%. The model 5 results showed the error in range of 0.774771% – 9.70528%. The model 6 results gave the error in range of 1.18119% – 8.73707%. And the model 7 showed the relative error in the range of 0.0810618% – 8.82717%. The good fit range of the relative error (ARE) for high precision models is usually

TABLE VIII: Results of elastic cross section by integration of our models of the differential cross section.

\sqrt{s}	Model 1	Model 2	Model 3	Model 4	Model 5	Model 6	Model 7	ISR [74]	2.76 TeV [75]	7 TeV [72]	8 TeV [73]	13 TeV [71]
	(mb)	(mb)	(mb)	(mb)	(mb)	(mb)	(mb)	(mb)	(mb)	(mb)	(mb)	(mb)
23 GeV	6.5266	6.32625	6.60557	6.71209	6.1923	6.39853	6.39189	-	-	-	-	-
23.5 GeV	6.63969	6.66799	6.64812	6.66571	6.51434	6.53946	6.63523	6.82	-	-	-	-
27.43 GeV	7.14003	7.71544	7.34718	7.05101	7.61527	7.54103	7.0634	-	-	-	-	-
30.7 GeV	7.38816	7.15672	7.07817	7.00381	7.66528	7.86892	7.29245	7.39	-	-	-	-
44.7 GeV	7.21617	7.6702	7.34404	7.07463	7.61901	7.70186	7.44081	7.45	-	-	-	-
52.8 GeV	7.23764	7.40069	7.27359	7.35688	7.20325	7.37242	7.47945	7.56	-	-	-	-
62.5 GeV	7.54864	7.72488	7.7626	7.71417	7.0159	7.09113	7.85378	7.77	-	-	-	-
200 GeV	10.11363	10.0696	10.0022	10.1906	10.2148	10.247	10.3973	-	-	-	-	-
800 GeV	12.08162	12.0289	12.067	12.0671	12.0981	12.0553	12.0042	-	-	-	-	-
2.76 TeV	21.7784	21.4749	20.7911	22.7031	21.6311	21.5425	23.2111	-	21.8 ± 1.4	-	-	-
7 TeV	23.4114	25.4306	24.4253	24.3276	24.6489	24.3124	27.6421	-	-	25.4 ± 1.1	-	-
8 TeV	26.6814	26.522	27.4732	26.554	26.8882	27.6492	27.1972	-	-	-	27.1 ± 1.4	-
13 TeV	31.0991	31.6471	31.5338	31.4935	31.459	31.7374	30.9749	-	-	-	-	31.0 ± 1.7
14 TeV	32.7335	32.0887	32.3486	32.44	31.2397	32.0094	32.5215	-	-	-	-	-
15 TeV	34.1479	34.1934	34.3307	34.7952	34.2409	34.3047	34.607	-	-	-	-	-
28 TeV	35.6335	36.0963	36.3509	36.0248	37.1658	36.2268	36.9525	-	-	-	-	-

TABLE IX: Relative error calculation of the σ_{el} results

\sqrt{s}	Model 1	Model 2	Model 3	Model 4	Model 5	Model 6	Model 7
	% Abs. Rel. Error	% Abs. Rel. Error	% Abs. Rel. Error	% Abs. Rel. Error	% Abs. Rel. Error	% Abs. Rel. Error	% Abs. Rel. Error
23.5 GeV	2.64384	2.22889	5.19177	2.26232	4.48182	4.11349	2.70924
30.7 GeV	0.0248985	3.1567	4.21962	5.22585	3.72503	6.48065	1.32003
44.7 GeV	3.13866	2.9557	1.42228	5.03852	2.26859	3.38067	0.123356
52.8 GeV	4.26402	2.10728	3.78849	2.68677	4.71892	2.48122	1.06548
62.5 GeV	2.84891	0.580695	0.0952381	0.718533	9.70528	8.73707	1.07825
2.76 TeV	0.0990826	1.49128	4.62798	4.14266	0.774771	1.18119	6.47294
7 TeV	7.82913	0.120472	3.8374	4.22205	2.95709	4.28189	8.82717
8 TeV	1.54461	2.13284	1.37712	2.01476	0.781651	2.02657	0.358672
13 TeV	0.319677	2.08742	1.72194	1.59194	1.48065	2.37871	0.0810618

considered to be $ARE < 5\%$. For global fits especially when covering a broad energy range (from ISR to LHC), ARE range is $5\% \leq ARE \leq 10\%$. Poor Fit Range corresponds to the $ARE > 15\%$ which indicates significant disagreement with data. In this study, the results of the total elastic cross section for all the seven models are found to be in ARE range of $0.0248985\% \leq ARE \leq 9.70528\%$. The lowest relative error range is found across the model 2 results of the total elastic cross section σ_{el} .

C. Total and Inelastic Cross Section

We extend the calculations of this study for the observable, total cross section σ_{tot} , using the optical theorem. The results of the total cross section σ_{tot} are obtained by the extrapolation of the models, at $t = 0$:

$$\sigma_{tot}^2 = \frac{16\pi(\hbar c)^2}{1 + \rho^2} \left(\frac{d\sigma}{dt} \right)_{t=0} \quad (26)$$

$$\sigma_{inel} = \sigma_{tot} - \sigma_{el} \quad (27)$$

The conversion factor $(\hbar c)^2 \simeq 0.38 \text{ GeV}^2 \text{ mbarn}$ is used in these σ_{tot} calculations. The ρ parameter values used for each energy along with the calculated total cross sections are given in Table 10. The calculations of the σ_{tot} relied mostly on the outcome of the models after their extrapolation at $t = 0$ with the determined fitted parameters values. The model 5 and 6 contained the power law factor in the first exponential term due to which the extrapolated values

of the $(d\sigma/dt)_{t=0}$ are drastically lowered and resulted in very lower values of total cross section σ_{tot} . When this factor is neglected in these models then σ_{tot} values increased while keeping other parameters same. The σ_{tot} results of model 5 and 6 have been shown after doing this modification in Table 10. The calculated results of the inelastic cross section σ_{inel} are given in Table 11. A comparison plot of σ_{el} , σ_{tot} and σ_{inel} is shown in Figure 8 for graphical visualization purposes of the results of these observables. The σ_{el} , σ_{tot} reference curves are obtained by joining the reference values of the Tables 8 and 10. The difference of these reference values is used to obtain a reference curve for inelastic cross section. It is evident from the Figure 8 that σ_{el} results from our models show very good agreement with σ_{el} reference values where available, and show quite reasonable values at the extrapolated energies. All the calculated σ_{el} values lie on the reference curve depicting very small or almost no major difference with the references points. Generally, σ_{tot} results of the models 1, 2, 3, 4 and 7 showed lesser difference with the reference values as compared to the models 5 and 6 which have shown least agreement among all the models. The results across the models 5 and 6 show the highest underestimation of σ_{tot} and are observed at the lowest level below the reference curve. The models 1, 2, 3 and 4 underestimated the total cross sections from c.m. energies 23 GeV - 62.5 GeV. And from c.m. energies 200 GeV to 28 TeV these models showed more agreement with the reference values. Among the models 1, 2, 3, and 4, the model 3 results showed least agreement at c.m energies 200 GeV to 28 TeV with the reference values. The results of models 1, 4, and 7 showed least difference from the reference values among all the models with the model 7 showing most agreement with reference values of σ_{tot} and its values almost appear on the reference curve. For the observable σ_{inel} , a similar trend can be observed in the Figure 8 across all the model results with the reference values. Among these models, the model 7 results for σ_{inel} are in most agreement with the reference values. It is important to observe that the calculated results showed rise in the observables, σ_{el} , σ_{tot} , and σ_{inel} with increasing c.m. energy for all the models. It is evident from Figure 8 that σ_{el} rises slowly as compared to the σ_{tot} with increasing c.m. energies. Subject to model-dependent theoretical interpretations, the ratio $\sigma_{\text{el}}/\sigma_{\text{tot}}$ can provide some information on the shape and opacity of proton. The consistent increase in this ratio with energy is frequently considered to be an indication of increase of proton size and opacity with energy [68]. The calculations of ratio, $\sigma_{\text{el}}/\sigma_{\text{tot}}$ by TOTEM have been reported in ref. [69]. Results of σ_{el} and σ_{tot} by our models are analyzed in this study for $\sigma_{\text{el}}/\sigma_{\text{tot}} \sim (\log(s))^{-n}$ behavior which is given in ref. [65] for elastic processes, with $n=1$, and is related to the shrinkage of the forward peak, described by approximating residue by a single exponential to obtain the differential cross section that has the similar s dependence which is introduced in our models. This ratio suggests that elastic fraction of the total scattering decreases with increasing c.m. energy indicating the decrease of purely elastic events which never entirely vanish, giving an indication that inelastic processes dominate at very high energies. At GeV energies (23 GeV - 800 GeV) the elastic cross-section comprises $\sim 15\text{--}20\%$ of the total cross-section. The ratio fits well with the $\sim \log(s)$ behavior. At LHC energies 2.76 TeV - 13 TeV, the ratio lies in the range $\sigma_{\text{el}}/\sigma_{\text{tot}} \sim 0.23 - 0.27$. Our results for the behavior, $\sigma_{\text{el}}/\sigma_{\text{tot}} \sim (\log(s))^{-1}$ show consistency especially for the model 7 at LHC energies of 2.76 TeV - 13 TeV and at the extrapolated energies of 14 TeV, 15 TeV and 28 TeV. This energy regime is very high so that the scattering is dominated by exchange of Pomeron that contributes to a logarithmic rise in σ_{tot} which is in accordance with the Froissart-Martin bound. However, at GeV energies which are very low than LHC energies, the ratio $\sigma_{\text{el}}/\sigma_{\text{tot}}$, shows inconsistency with the $(\log(s))^{-1}$ behavior. In this study, the deviations in σ_{tot} and σ_{inel} values from their reference values which have been observed in the results of the models can be attributed to the lack of explicit constraints in the forward scattering region in the models. It is usually found that model-independent parametrizations which are made to fit the mid- $|t|$ region may not constrain the forward limit effectively which can affect the calculations of σ_{tot} and σ_{inel} . Also the model parameters values have been obtained through non-linear fitting of the models with the data with no initial values which leads to many solutions, subsequently, affecting the results of the observables found by the models. We adopted the simple parameters choices for the functions $A(s,t)$ and $B(s,t)$ for t dependence in our models to reduce the number of free parameters and for other reasons which resulted in oversimplification in terms of t dependence which affected the extrapolation at $t = 0$. Moreover, it can be understood that modifications related to certain physical constraints are required in the composite exponential structures of the models to better represent the scattering amplitude contributions thereby overcoming the limitations in the calculations of σ_{tot} and σ_{el} observables. These are also required for correlation with other models, and other advances in the modeling of the differential cross section. In the present study, we are not interested in investigating the energy dependence of other free parameters of our models. It can be very significant to investigate the scaling patterns in the free parameter values obtained in this study. Moreover, it will be very useful to study how their extracted values relate to energy and other physical parameters used in other theoretical and phenomenological approaches.

The models of $\frac{d\sigma}{dt}$ used in this study can be used to predict several important observables that are very significant in understanding of proton dynamics and structure of proton in pp elastic scattering at high energies. For instance, the local slope parameter or logarithmic slope $B(t)$ of the differential cross section, defined by taking s fixed at $s = s_0$ in

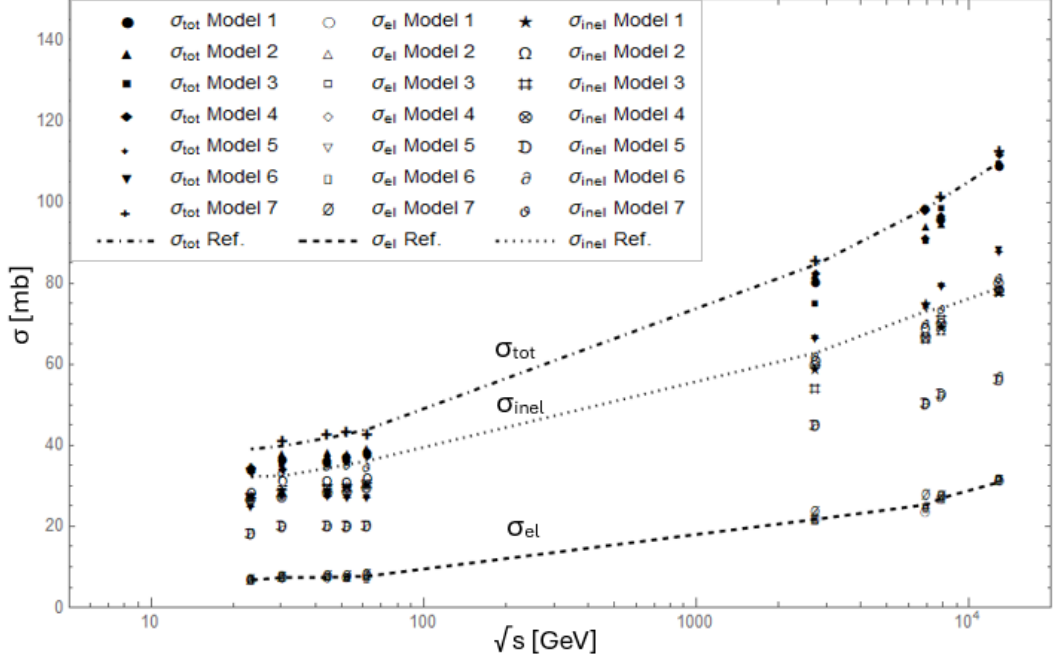


FIG. 8: Graphical comparison of total, elastic, and inelastic cross-section calculation results by our models presented with the reference values (as shown in Tables 8, 10 and 11) as function of the centre-of-mass energy. The results across 23.5 GeV, 30.7 GeV, 44.7 GeV, 52.8 GeV, 62.5 GeV, 2.76 TeV, 7 TeV, 8 TeV, and 13 TeV energies are shown. The dotted dashed line represents the reference curve of σ_{tot} . The dotted line represents the reference curve of σ_{inel} . And the dashed line represents the reference curve of σ_{el} . These reference curves are obtained by joining only the reference points at the aforementioned energies.

our models which are s and t dependent. $B(t)$ is obtained as

$$B(t) = \frac{d}{dt} \left[\ln \left(\left| \frac{d\sigma(s,t)}{dt} \right|_{s=s_0} \right) \right], \quad (28)$$

which reflects the t -dependent variation of the elastic scattering. This t -dependent slope parameter for pp and $p\bar{p}$ data has been used in ref. [7] to investigate Odderon effect by finding $B(t)_{pp} \neq B(t)_{p\bar{p}}$. In ref. [70], an indication of two substructures of different sizes in proton is given at low and high energy domains by the t dependent slope parameter. By the directions followed in ref. [70], the $B(s)$ slope parameter can be taken as $B(s) \equiv B(s, t=0)$ which can be related to ρ parameter, σ_{el} and σ_{tot} thereby leading to estimate scaling properties of shadow profile which are very significant to study structure and dynamics of proton at high energies. These $B(s)$ and $B(t)$ parameters obtained by our models can offer insights into changes in interaction geometry with their dependence on mandelstam variables s and t , respectively. The increase in the slope parameter with \sqrt{s} as a feature of $\frac{d\sigma}{dt}$ is linearly related with the radius of proton [9]. The $\frac{d\sigma}{dt}$ models can also be used to predict the differential curvature and dip behavior by estimating the second derivative of $\ln(d\sigma/dt)$ by keeping s fixed at $s = s_0$, thereby estimating $C(t)$ which gives access to effects related to curvature of the cross section [48]:

$$C(t) = \frac{d^2}{dt^2} \left[\ln \left(\left| \frac{d\sigma(s,t)}{dt} \right|_{s=s_0} \right) \right], \quad (29)$$

The $C(t)$ parameter is very important in analysis of the dip-bump region and deviations from simple exponential behavior.

TABLE X: Results of the total cross section σ_{tot} by extrapolation of our models at $t = 0$.

\sqrt{s}	ρ	Model 1	Model 2	Model 3	Model 4	Model 5	Model 6	Model 7	ISR [74]	2.76 TeV [75]	7 TeV [72]	8 TeV [73]	13 TeV [71]	[47]
		σ_{tot}	σ_{tot}	σ_{tot}	σ_{tot}	σ_{tot}	σ_{tot}	σ_{tot}	σ_{tot}	σ_{tot}	σ_{tot}	σ_{tot}	σ_{tot}	σ_{tot}
		(mb)	(mb)	(mb)	(mb)	(mb)	(mb)	(mb)	(mb)	(mb)	(mb)	(mb)	(mb)	(mb)
23 GeV	0.20	33.2336	26.1475	32.9198	32.6293	24.6788	24.0305	34.4787	-	-	-	-	-	-
23.5 GeV	0.24	33.8358	34.4178	33.4971	33.1993	24.5107	24.5614	33.8546	39.13 ± 0.32	-	-	-	-	-
27.43 GeV	0.22	35.9199	33.5109	35.6143	34.106	31.8161	26.6363	37.0694	-	-	-	-	-	-
30.7 GeV	0.23	36.1188	37.909	34.9297	34.117	27.4689	27.3694	40.6695	39.91 ± 0.33	-	-	-	-	-
44.7 GeV	0.21	35.9753	38.2821	36.3573	35.1343	27.353	27.3683	42.4822	41.89 ± 0.32	-	-	-	-	-
52.8 GeV	0.19	36.7937	37.9199	36.4871	35.8055	26.9674	26.9482	42.8629	42.85 ± 0.33	-	-	-	-	-
62.5 GeV	0.17	37.7253	39.0542	37.9971	37.201	26.8442	26.8527	42.4021	44.0	-	-	-	-	-
200 GeV	0.17	50.2963	50.8963	49.4038	47.7857	35.3484	35.1759	51.5503	-	-	-	-	-	-
800 GeV	0.10	61.577	57.3945	61.3998	61.9122	40.6869	40.2516	61.8687	-	-	-	-	-	-
2.76 TeV	0.14	80.1842	81.8242	74.4543	82.4611	66.2536	66.1486	85.1398	-	84.7 ± 3.3	-	-	-	-
7 TeV	0.12	98.0091	93.8196	90.1696	91.0053	74.6107	74.0505	97.6735	-	-	98.6 ± 2.2	-	-	-
8 TeV	0.12	95.3942	94.6602	98.0982	96.629	79.0808	79.2133	100.928	-	-	-	101.7 ± 2.9	-	-
13 TeV	0.09	108.629	109.529	109.022	111.696	87.3737	88.2038	112.366	-	-	-	-	110.6 ± 3.4	-
14 TeV	0.108	122.689	119.65	90.82	120.246	97.3395	94.9042	122.839	-	-	-	-	-	108.1
15 TeV	0.109	123.460	121.929	92.588	123.991	100.533	102.14	124.913	-	-	-	-	-	109.1
28 TeV	0.114	134.549	132.356	102.644	134.465	108.042	110.617	132.873	-	-	-	-	-	118.5

TABLE XI: Results of inelastic cross section σ_{inel} .

\sqrt{s}	Model 1	Model 2	Model 3	Model 4	Model 5	Model 6	Model 7	ISR [74]	2.76 TeV [75]	7 TeV [72]	8 TeV [73]	13 TeV [71]
	σ_{inel}	σ_{inel}	σ_{inel}	σ_{inel}	σ_{inel}	σ_{inel}	σ_{inel}	σ_{inel}	σ_{inel}	σ_{inel}	σ_{inel}	σ_{inel}
	(mb)	(mb)	(mb)	(mb)	(mb)	(mb)	(mb)	(mb)	(mb)	(mb)	(mb)	(mb)
23 GeV	26.707	19.8212	26.3142	25.9172	18.4865	17.632	28.0868	-	-	-	-	-
23.5 GeV	27.1961	27.7499	26.8489	26.5336	17.9964	18.022	27.2193	29.07 ± 0.32	-	-	-	-
27.43 GeV	28.7798	25.7954	28.2671	27.055	24.2008	19.0953	30.006	-	-	-	-	-
30.7 GeV	28.7307	30.7522	27.8515	27.1132	19.8036	19.5005	33.377	32.52 ± 0.33	-	-	-	-
44.7 GeV	28.7591	30.6119	29.0133	28.0597	19.734	19.6664	35.0414	34.44 ± 0.32	-	-	-	-
52.8 GeV	29.5561	30.5192	29.2135	28.4486	19.7642	19.5757	35.3834	35.29 ± 0.33	-	-	-	-
62.5 GeV	30.1767	31.3293	30.2345	29.4868	19.8283	19.7615	34.5484	$36.23 \pm$	-	-	-	-
200 GeV	40.1827	40.8267	39.4016	37.5951	25.1336	24.9289	41.153	-	-	-	-	-
800 GeV	49.4954	47.3249	49.3709	49.8451	28.5888	28.1963	49.8645	-	-	-	-	-
2.76 TeV	58.4058	60.3493	53.6632	59.758	44.6225	44.6061	61.9287	-	62.8 ± 2.9	-	-	-
7 TeV	74.5977	68.389	62.7443	66.6777	49.9618	49.7381	70.0314	-	-	70.5 ± 2.9	-	-
8 TeV	69.1446	68.1382	70.625	70.075	52.1927	51.5641	73.7308	-	-	-	73.74 ± 0.09	-
13 TeV	77.5295	77.8817	77.488	80.1617	55.9147	56.4664	81.3911	-	-	-	-	79.1 ± 1.8
14 TeV	89.9554	87.5616	58.4715	87.8062	66.0998	62.8948	90.3177	-	-	-	-	-
15 TeV	89.3124	87.5987	58.2573	89.1961	66.2917	67.8348	90.3059	-	-	-	-	-
28 TeV	98.9157	96.2595	66.2927	98.4403	70.8761	74.3899	95.9204	-	-	-	-	-

IV. CONCLUSION

Our primary motivation for investigating the inverse problem as a source of experimental information, suitable for model development, and potential linkages with QCD evolved from the absence of a pure QCD description of the pp elastic scattering data and well-defined physical scenarios associated with a wide range of phenomenological models. For this purpose, we have performed a global comparative analysis of the elastic pp scattering across a wide range of energies, extending from the lower ISR energies to the higher LHC energies and at the extrapolated energies, by fitting seven composite models of $\frac{d\sigma}{d|t|}$. Each model incorporated distinct exponential structures to represent the composite behavior of the differential cross section across different kinematic regions from the forward peak at small- $|t|$, through the diffractive dip, to the high- $|t|$ tail dominated by hard scattering processes. Our model fits reproduced the important features such as the forward exponential fall-off and the dip-bump structure. The behavior of the dip is well produced in the graphical representation of the data by the fits of our models. The dip position is found to be moving towards smaller $|t|$ values and becoming shallower with increasing center-of-mass energy. This physical trend indicates the

increasing blackness and size of the proton at higher energies, consistent with the expected gluonic saturation effects and the shrinkage of the forward peak. The high- $|t|$ behavior which is governed by the inner quark structure is also accurately described in the multi-exponential contributions of our models. The calculated total elastic cross sections, evaluated through numerical integration of the fitted models, showed good consistency with known measurements and with established predictions for the ISR, TOTEM experimental data and also at extrapolated energies. The results of the total and inelastic cross section are found to be in good agreement with most of our models. The rise in elastic, inelastic and total cross sections is observed in their estimations by our models with increasing center of mass energies in both GeV and TeV energy domains. The analysis of the the ratio σ_{el}/σ_{tot} showed the that our results produced expected patterns at GeV and TeV energy domains. However, the calculations of the observables, σ_{tot} and σ_{inel} showed differences with the calculations by other models which indicated the limitation of some of our models. However, it is crucial to consider these limitations as suggestions for developments and improvements. Based on the consideration related to the extrapolations of these models, these models can be considered in three groups. The group 1 contains the models 1-4, the group 2 contains the models 5 and 6, and the group 3 contains the model 7. It is found that with almost same fitting agreement in the graphical representation of all the data, very small χ^2 values that are very close to each other, and very similar results of σ_{el} that show strong agreement with the reference values, each group has a different level of compatibility with the reference values of σ_{tot} and σ_{inel} . It is found that the group 1 shows more underestimation of σ_{tot} and σ_{inel} at the GeV energy domains and less overestimations at TeV energy domains as compared to group 3. While the group 2 shows the highest underestimation of the σ_{tot} and σ_{inel} among all the groups at GeV energy domain. Moreover, dependent on the fitting agreement with all the data, lesser difference with reference values of σ_{el} , σ_{tot} and σ_{inel} at most of the energies, and other considerations discussed in section III, the group 3 (model 7) is found to be the most reasonable among all the models. It is understood from present analysis that efficient modeling strategy demands detailed investigation of different analyses and results. Generally, the good fitting agreement of our models with previous significant works that includes those based on the Bialas Bazdak (BB) model, impact picture, the FMO approach, emphasizes the physical relevance of our parametrizations of the differential cross section. It reinforces the understanding that the internal structure of proton and the dynamics of elastic scattering can be consistently described by modeling of the differential cross sections. This study, therefore, provides a basis for future refinements of phenomenological models and offers predictive strength for upcoming experiments at higher and intermediate energies.

V. RECOMMENDATIONS AND FUTURE WORK

In the present study, the composite exponential models which have been used to effectively describe the differential cross section behavior of pp elastic scattering across a wide energy range can be further improved in the aforementioned directions of section III. The parameters can be modified in terms of mandelstam variables s and t especially by developing parametrizations that have more effective theoretical roots. It is recommended to combine phenomenological fitting of these models with theoretical models such as eikonal frameworks and QCD-based saturation approaches to explain the underlying dynamics. These models can be considered for further validation with the availability of new data from the LHC and future colliders like the FCC, particularly at very low and very high- $|t|$. The use of machine learning techniques may also offer improved predictive capabilities. We are hopeful that extensions of this study along the highlighted directions can promise richer insights into hadronic physics.

A. Acknowledgment

Muhammad Saad Ashraf is thankful to Dr. Nosheen Akbar and Dr. Sarwat Zahra for their guidance as supervisors which is crucial for the successful completion of this work.

REFERENCES

-
- [1] A. Donnachie and P.V. Landshoff, (1992) "Total cross sections", *Phy. Lett. B* **296**, 227-232.

- [2] Block, M. M. and Halzen, F., (2011) "Forward hadronic scattering at 7 TeV: An update on predictions for the LHC", Phys. Rev. D **83**.
- [3] A. Donnachie and P.V. Landshoff, (2013) " pp and $\bar{p}p$ total cross sections and elastic scattering", Phys. Lett. B **727**, 500-505.
- [4] Donnachie, S. and Dosch, G. and Landshoff, P. and Nachtmann, O., (2002) "Pomeron Physics and QCD", Cambridge University Press.
- [5] Forshaw, J.R. and Ross, D.A., (1997) "Quantum Chromodynamics and the Pomeron", Cambridge University Press.
- [6] E. Nagy et al., (1979) "Measurements of elastic proton-proton scattering at large momentum transfer at the CERN intersecting storage rings", Nucl. Phys. B **150**, 221-267.
- [7] Antchev, G. et al., (2020) "Elastic differential cross-section $d\sigma/dt$ at $\sqrt{s} = 2.76$ TeV and implications on the existence of a colourless C-odd three-gluon compound state", Eur. Phys. J. C **80**, CERN-EP-2018-341, TOTEM-2018-002.
- [8] Antchev, G. et al., (2013) "Measurement of proton-proton inelastic scattering cross-section at $\sqrt{s}=7$ TeV", Europhysics Letters **101**, 21003.
- [9] The TOTEM Collaboration and Antchev, G. et al., (2011) "Proton-proton elastic scattering at the LHC energy of 7 TeV", Europhysics Letters **95**, 41001.
- [10] The TOTEM Collaboration and Antchev, G. et al., (2022) "Characterisation of the dip-bump structure observed in proton-proton elastic scattering at $\sqrt{s} = 8$ TeV", Eur. Phys. J. C **82**, 263.
- [11] Antchev, G. et al., (2019) "Elastic differential cross-section measurement at $\sqrt{s}=13$ TeV by TOTEM", Eur. Phys. J. C **79**, 861.
- [12] Abazov, V. M. et al., (2021) "Odderon Exchange from Elastic Scattering Differences between pp and $\bar{p}p$ Data at 1.96 TeV and from pp Forward Scattering Measurements", Phys. Rev. Lett. **127**, 062003.
- [13] Marco Bozzo et al., (1984) "Low momentum transfer elastic scattering at the CERN proton-antiproton collider", Phys. Lett. B **147**, 385-391.
- [14] UA4 Collaboration, (1985) "Elastic Scattering at the CERN SPS Collider Up to a Four Momentum Transfer of 1.55 GeV^2 ", Phys. Lett. B **155**, 197.
- [15] CDF Collaboration, (1994) "Measurement of small angle $\bar{p}p$ elastic scattering at $\sqrt{s} = 546 \text{ GeV}$ and 1800 GeV ", Phys. Rev. D, **50**, 5518.
- [16] E710 Collaboration, (1988) "Measurement of b , the Nuclear Slope Parameter of the $\bar{p}p$ Elastic Scattering Distribution at $\sqrt{s} = 1800 \text{ GeV}$ ", Phys. Rev. Lett., **61**, 525.
- [17] E710 Collaboration, (1989) "Measurement of the $\bar{p}p$ Total Cross-Section at $\sqrt{s} = 1.8 \text{ TeV}$ ", Phys. Rev. Lett., **63**, 2784.
- [18] E710 Collaboration, (1992) "Measurement of ρ , the ratio of the real to imaginary part of the $\bar{p}p$ forward elastic scattering amplitude, at $\sqrt{s} = 1.8 \text{ TeV}$ ", Phys. Rev. Lett., **68**, 2433.
- [19] Aaboud, M. and et al., (2016) "Measurement of the total cross section from elastic scattering in pp collisions at $\sqrt{s} = 8 \text{ TeV}$ with the ATLAS detector", Phys. Rev. Lett., **117**, 182002.
- [20] Adamczyk, L. and et al., (2016) "Single spin asymmetry A_N in polarized proton-proton elastic scattering at $\sqrt{s} = 200 \text{ GeV}$ at RHIC", Phys. Rev. Lett., **719**, 62-69.
- [21] M. Froissart, (1961) "Asymptotic behavior and subtractions in the Mandelstam representation", Phys. Rev., **123**, 1053.
- [22] P. Gauron, L. Lukaszuk and B. Nicolescu, (1992) "Consistency of the maximal odderon approach with the QFT constraints", Phys. Lett. B, **294**, 298.
- [23] M. M. Block et al., (1994) "The High-energy behavior of the forward scattering parameters σ_{total} , ρ and B ", arXiv:hep-ph/9412306, 73-78.
- [24] J. R. Cudell et al, (2002) "Hadronic scattering amplitudes: Medium-energy constraints on asymptotic behavior", Phys. Rev. D, **65**, 074024.
- [25] COMPETE Collaboration, (2002) "Benchmarks for the forward observables at RHIC, the Tevatron Run II and the LHC", Phys. Rev. D, **89**, 201801.
- [26] TOTEM Collaboration, (2018) "First determination of the ρ parameter at $\sqrt{s} = 13 \text{ TeV}$ — probing the existence of a colourless three-gluon bound state", arXiv:1812.04732 [hep-ex].
- [27] M. M. Islam, (2018) "<https://slac.stanford.edu/econf/C111215/papers/islam.pdf>".
- [28] I.M. Dremin and V.A. Nechitailo, (2013) "Proton periphery activated by multiparticle dynamics", Nuc. Phys. A, **916**, 241-248.
- [29] Nekrasov, M. L., (2023) " pp elastic scattering at ISR and LHC energies", Phys. Rev. D, **108**, 034028.
- [30] Gelis, F. et al., (2010) "The Color Glass Condensate", Ann. Rev. Nucl. Part. Sci., **60**, 463-489.
- [31] Saleem, M. and Fazal-e-Aleem, (1980), "Dipole Pomeron and Proton-Proton Elastic Scattering at High Energies", Austr. Jour. Phys., **33**, 481.
- [32] R. N. Cahn, (1982), "Coulomb-Hadronic Interference in an Eikonal Model", Z. Phys. C., **15**, 253-260.
- [33] D. A. Fagundes, M. J. Menon, (2012), "Total Hadronic Cross Section and Elastic Slope: An Almost Model-Independent Connection", Nucl. Phys. A, **880**, 1-15.
- [34] V. Kundrať and M. Lokajčěk, (1992), "High-energy elastic hadron scattering in Coulomb and hadronic regions", Phys. Rev. D, **46**, 4087-4090.
- [35] Antchev G. et al., (2015), "Evidence for non-exponential elastic proton-proton differential cross-section at low $|t|$ and $\sqrt{s} = 8 \text{ TeV}$ by TOTEM", Nucl. Phys. B, **899**, 527-546.
- [36] Antchev, G. and others (TOTEM Collaboration), (2019), "Elastic Differential Cross-Section Measurement at 13 TeV by TOTEM", Eur. Phys. J. C, **79**, 103.

- [37] Kohara, A. K. and Ferreira, E. and Kodama, T., (2017), "Amplitudes for High-Energy Proton-Proton Elastic Scattering", *Eur. Phys. J. C*, **77**, 877.
- [38] Jenkovszky, L'aszl'o and Szanyi, Istv'an, (2018), "Elastic and inelastic diffraction at the LHC", *EPJ Web Conf.*, **172**, 06004.
- [39] E. Martynov, (2018), "Did TOTEM experiment discover the Odderon?", *Phys. Lett. B*, **778**, 414-418.
- [40] O.V. Selyugin, (2015), "Nucleon structure and the high energy interactions", *Phys. Rev. D*, **91**, 113003.
- [41] O.V. Selyugin, (2012), "GPDs of the nucleons and elastic scattering at high energies", *Eur. Phys. J. C*, **72**, 2073.
- [42] O.V. Selyugin, (2019), "New feature in the differential cross sections at 13 TeV measured at the LHC", *Phys. Lett. B*, **797**, 134870.
- [43] O.V. Selyugin, (2024), "New properties of elastic pp and $p\bar{p}$ scattering at high energies", *Eur. Phys. J. C*, **84**, 649.
- [44] Xie. Wei, Watanabe. Akira, Huang. Mei, (2019), "Elastic proton-proton scattering at LHC energies in holographic QCD", *J. of High Energy Phys.*, **2019**, 53.
- [45] R.J.N. Phillips and V. Barger, (1973), "Model independent analysis of the structure in pp scattering", *Phys. Lett. B*, **46**, 412-414.
- [46] Gonçalves, V.P., Silva, P.V.R.G., (2015), "The Phillips–Barger model for the elastic cross section and the Odderon", *Eur. Phys. J. C*, **79**, 237.
- [47] Nemes, F. and C. org, T. and Csanad, M., (2015), "Excitation function of elastic pp scattering from a unitarily extended Bialas-Bzdak model", *Int. J. Mod. Phys. A*, **30**, 1550076.
- [48] Csörgő, Tamás and Hegyi, Sandor and Szanyi, István, (2023), "Lévy α -Stable Model for the Non-Exponential Low- $|t|$ Proton–Proton Differential Cross-Section", *Universe*, **9**, 361.
- [49] Praszalowicz, M. et al., (2025), "Scaling of the elastic proton-proton cross-section", *arXiv.2501.08398[hep-ph]*.
- [50] Baldenegro, C. et al., (2024), "Scaling laws of elastic proton-proton scattering differential cross sections", *Phys. Lett. B*, **856**, 138960.
- [51] M. M. Block and F. Halzen, (2011), "New fit to high-energy pp and $p\bar{p}$ scattering data", *Phys. Rev. D*, **83**, 077901.
- [52] V. V. Anisovich et al., (2014), "Impact parameter analysis of pp and $p\bar{p}$ scattering", *Phys. Rev. D*, **90**, 074005.
- [53] S. Dulat et al., (2016), "New Parton Distribution Functions from the CT14 Global Analysis", *Phys. Rev. D*, **93**, 033006
- [54] TOTEM Collaboration, (2013), "Luminosity-independent measurement of the total proton-proton cross-section at $\sqrt{s} = 8$ TeV", *Phys. Rev. Lett.*, **111**, 012001.
- [55] Pierre Auger Collaboration, (2016), "Testing Hadronic Interactions at Ultra-High Energies", *Phys. Rev. Lett.*, **117**, 192001.
- [56] S. Ostapchenko, (2019), "QGSJET-II: physics, recent improvements, and results for air showers", *EPJ Web Conf.*, **208**, 11002.
- [57] Grau, A. et al., (2019), "The elastic differential pp cross-section at 13 TeV: an empirical model analysis", *EPJ Web Conf.*, **206**, 06003.
- [58] Dremin, I. M., (2013), "Elastic pp scattering from the optical point to past the dip: An empirical model analysis", *Phys. Lett. B*, **720**, 83-86.
- [59] Abada, A. et al., (2019), "FCC Physics Opportunities", *Eur. Phys. J. C*, **79**, 474.
- [60] Albertsson K. et al., (2019), "Machine Learning for High-Energy Physics Applications", *arXiv:1807.02876 [physics.comp-ph]*.
- [61] U. Amaldi et al., (1980), "Impact parameter interpretation of proton-proton scattering from a critical review of all ISR data", *Nuc. Phys. B*, **166**, 301-320.
- [62] Bourrely, C. and Soffer, Jacques and Wu, Tai Tsun, (1979), "A New Impact Picture for Low and High-Energy Proton Proton Elastic Scattering", *Phys. Rev. D*, **19**, 3249.
- [63] Bence, N. et al., (2020), "Froissaron and Maximal Odderon with spin-flip in pp and $p\bar{p}$ high energy elastic scattering", *arXiv:2010.11987 [hep-ph]*.
- [64] Stanley J. Brodsky and Glennys R. Farrar, (1973), "Scaling Laws at Large Transverse Momentum", *Phys. Rev. Lett.*, **31**, 1153-1156.
- [65] Collins, P. D. B., (1977), "An Introduction to Regge Theory and High Energy Physics", Cambridge University Press.
- [66] Jenkovszky, László and Schicker, Rainer and Szanyi, István, (2022) "Regge Models of Proton Diffractive Dissociation Based on Factorisation and Structure Functions", *Entropy*, **24**, 7.
- [67] L. Adamczyk et al. (STAR Collaboration), (2013) "Single spin asymmetry A_N in polarized proton-proton elastic scattering at $\sqrt{s} = 200$ GeV", *Phys. Lett. B*, **719**, 62-69.
- [68] Adamczyk, Leszek., (2015) "Measurement of the Total Cross Section in Proton Proton Collisions at $\sqrt{s}=7$ TeV with the ALFA Sub-Detector of ATLAS", *Phys. Lett. B*, **DIS2015**, 61.
- [69] Antchev, G. et al. (TOTEM collaboration), (2013) "Luminosity-independent measurements of total, elastic and inelastic cross-sections at $\sqrt{s} = 7$ TeV", *EPL*, **101**, 2, 21004.
- [70] Csorgo T. et al., (2021) "Evidence of Odderon-exchange from scaling properties of elastic scattering at TeV energies", *Eur. Phys. J. C*, **81**, 180.
- [71] Anchteev G. et al., (2019) "First measurement of elastic, inelastic and total cross-section at TeV by TOTEM and overview of cross-section data at LHC energies", *Eur. Phys. J. C*, **79**.
- [72] Anchteev G. et al., (2013) "Measurement of proton-proton elastic scattering and total cross-section at $\sqrt{s} = 7$ TeV", *EPL*, **101**, 21002.
- [73] Antchev, G. et al., (2013) "Luminosity-Independent Measurement of the Proton-Proton Total Cross Section at $\sqrt{s} = 8$ TeV", *EPL*, **111**, 012001.

- [74] Baksay, L. et al., (1978) "Measurement of the Proton Proton Total Cross-Section and Small Angle Elastic Scattering at ISR Energies", Nucl. Phys. B, **141**, 1-28.
- [75] Cafagna, Francesco S., (2021) "Latest results for Proton-Proton Cross Section Measurements with the TOTEM experiment at LHC", PoS, **ICRC2019**, 207.